

A Pulsating Heat Pipe Based Thermal Management System for
Lithium-ion Batteries

by

Jianyu Liu

A thesis submitted to the Faculty of Graduate and Postdoctoral Affairs in partial fulfillment of the requirements for the degree of

Master of Applied Science

in

Mechanical Engineering

Carleton University
Ottawa, Ontario

© 2021

Jianyu Liu

Abstract

Lithium-ion batteries are widely adopted as portable energy storage devices due to their high energy capacity and relatively lightweight. Under high-intensity usage, an effective thermal management system is essential to control battery pack temperature within the desired range to guarantee battery safety and ensure a proper life cycle. This study developed a pulsating heat pipe (PHP) based thermal management system to promote battery temperature control. The system was tested for a large battery pack (2 kWh) under mild and severe ambient conditions via ANSYS Fluent simulation. A sensitivity study identified optimal PHP dimensions regarding the battery pack. The performance of PHP for both small and large scales was also evaluated. The system's effectiveness was compared to classical battery thermal management (BTM) systems such as forced air cooling, sidewall water cooling, and traditional heat pipes. The results demonstrated that the developed PHP-based passive cooling system effectively controls temperature, saves space, and reduces power consumption.

Acknowledgments

First and foremost, I would like to express my deepest gratitude to my supervisor: Prof. Jie Liu, who made this research work possible. Without his patient guidance and enthusiastic supervision, this thesis would not exist. He supported and guided me throughout the entire master program and always encouraged me to develop new ideas.

I would also take this opportunity to express my appreciation to all those who have helped me to complete this task. I would like to thank Dr. Rui Zhao, whose approach to research has forever changed mine. Shengcai Deng, another student in the research group, for his tremendous encouragement and support.

My completion of this project could not be accomplished without the support of my loving parents. Their constant encouragement throughout the course of this thesis is much appreciated and duly noted.

Contents

| | |
|--|------------|
| Abstract..... | ii |
| Acknowledgments | iii |
| List of Tables | v |
| List of Figures..... | vi |
| Nomenclature | ix |
| Chapter 1: Introduction | 1 |
| 1.1 Overview..... | 1 |
| 1.2 Objectives | 2 |
| 1.3 Thesis Outline | 4 |
| Chapter 2: Literature Review..... | 5 |
| 2.1 Lithium-ion Battery and the Thermal Issues..... | 5 |
| 2.2 Battery Thermal Management Systems | 8 |
| 2.2.1 Active Thermal Management System..... | 8 |
| 2.2.2 Passive Thermal Management System..... | 14 |
| 2.3 Summary | 19 |
| Chapter 3: Mathematical Modeling and Simulation Setup | 20 |
| 3.1 Simulation Setup..... | 20 |
| 3.2 Thermal Model Setup | 22 |
| 3.3 Grid Independence Study..... | 28 |

| | |
|--|-----------|
| 3.4 Fluent Modeling..... | 32 |
| Chapter 4: The Evaluation of Pulsating Heat Pipe Cooling Performance on Li-ion Battery | 38 |
| 4.1 Pulsating Heat Pipe Sensitivity Study..... | 38 |
| 4.1.1 Effect of Wall Thickness..... | 38 |
| 4.1.2 Effect of Condensation Length | 41 |
| 4.2 Comparison of Thermal Management Systems | 45 |
| 4.2.1 PHP vs. Active BTM system | 45 |
| 4.2.2 PHP vs. Heat Pipes..... | 53 |
| 4.3 Summary | 57 |
| Chapter 5: The Evaluation of Large Pulsating Heat Pipe Cooling Performance on Li-ion Battery..... | 58 |
| 5.1 Pulsating Heat Pipe Simulation..... | 58 |
| 5.2 Summary | 68 |
| Chapter 6: Conclusion and Future Works..... | 69 |
| 6.1 Conclusion | 69 |
| 6.2 Future Works | 71 |
| Bibliography | 72 |

List of Tables

| | |
|---|----|
| Table 1. Thermal characteristics of different inter-cell spacing battery modules [13] | 13 |
| Table 2. Specification of the $\text{LiNi}_x\text{Co}_y\text{Al}_{1-x-y}\text{O}_2$ battery. | 21 |
| Table 3. Battery specific heat concerning temperature [14]. | 24 |
| Table 4. Formulas of \mathbf{Sm}, \mathbf{l} and \mathbf{Sm}, \mathbf{v} | 27 |
| Table 5. Mesh quality study..... | 31 |
| Table 6. Description of the phases | 32 |
| Table 7. Details of numerical simulation..... | 33 |
| Table 8. Relaxation factors. | 35 |
| Table 9. Issues for different time steps | 36 |
| Table 10. Mesh quality summary for the liquid cooling system..... | 45 |
| Table 11. Mesh quality summary for the forced-air cooling system. | 48 |
| Table 12. Mesh quality summary for traditional heat pipe-based cooling system. | 54 |
| Table 13. Thermodynamic parameters of the 60 Ah battery cell at different rates [41]..... | 54 |
| Table 14. Mesh quality summary for large-scale PHP-based cooling system..... | 59 |

List of Figures

Chapter 2:

| | |
|---|----|
| Figure 2.1 Performance of common batteries: (a) LiCoO ₂ ; (b) LiFePO ₄ ; (c) LiNi _x Co _y Al _{1-x-y} O ₂ [5]..... | 6 |
| Figure 2.2 (a) Multi-layered core configuration in a lithium-ion battery; (b) lithium electrochemical reaction during operation [8]..... | 7 |
| Figure 2.3 (a) Cooling system demonstration; (b) structure and geometry of the silica-liquid cooling plate [12]..... | 10 |
| Figure 2.4 Schematic of the cooling system with different flow directions [12]. | 11 |
| Figure 2.5 Temperature nephograms of the battery at different flow directions [12]. | 11 |
| Figure 2.6 Explanation of fan and opening locations [13]..... | 12 |
| Figure 2.7 Temperature distribution of different battery packs [13]. | 13 |
| Figure 2.8 (a) Schematic of “U-type” flow battery pack; (b) Schematic of “Z-type” flow battery pack [14]. | 14 |
| Figure 2.9 Geometry of the battery module and thermal management system [15]..... | 15 |
| Figure 2.10 Schematic illustrations of four BTM systems: (a) horizontal heat pipes with cooling fan; (b) vertical heat pipes with natural cooling; (c) heat pipes in the thermostat water bath; (d) horizontal heat pipes with wet cooling system [16]..... | 16 |
| Figure 2.11 Photographs of the thermal test cells and components [17]..... | 18 |

Chapter 3:

| | |
|---|----|
| Figure 3.1 PHP thermal management system on 29 Ah battery pack: (a) small-scale PHP; (b) large-scale PHP..... | 22 |
|---|----|

| | |
|---|----|
| Figure 3.2 Grid dependency test by the average velocity..... | 28 |
| Figure 3.3 Grid dependency test by maximum velocity..... | 29 |
| Figure 3. 4 A small section plan view of: (a)PHP meshed in Fluent; (b) battery meshed in Fluent; (c) air cooling meshed in Fluent; (d) water cooling channel meshed in Fluent..... | 30 |
| Figure 3.5 Grid independency test on the battery pack. | 31 |
| Figure 3. 6 Fluent battery model setup | 34 |
| Figure 3. 7 Liquid distribution at t = 1 s, 3 s, 5 s, 8s, 10 s, respectively..... | 37 |
| Chapter 4: | |
| Figure 4.1 Battery temperature by different wall thickness at different ambient conditions. | 39 |
| Figure 4. 2 Temperature difference with respect to the wall thickness at different ambient conditions..... | 40 |
| Figure 4.3 Wall temperature against different wall diameters [30]. | 41 |
| Figure 4. 4 Variation of thermal resistance with heat input [39]..... | 42 |
| Figure 4.5 Battery temperature profile with different condenser lengths at both standard and abnormal ambient conditions..... | 43 |
| Figure 4.6 Battery ΔT profile with an ambient temperature of 25 °C. | 44 |
| Figure 4.7 Battery ΔT profile with an ambient temperature of 40 °C. | 44 |
| Figure 4.8 Battery temperature vs. time profile for PHP and liquid cooling at a discharge rate of 1C, at an ambient temperature of 25 °C. | 46 |
| Figure 4.9 Battery temperature vs. time profile for PHP and liquid cooling at a discharge rate of 1C, at an ambient temperature of 40 °C. | 47 |
| Figure 4. 10 Battery temperature vs. time profile for PHP and air cooling at a discharge rate of 1C, at an ambient temperature of 25 °C. | 49 |

| | |
|---|----|
| Figure 4.11 Numerical simulation profiles of temperature distribution inside battery pack with (a) PHP-based BTM system; (b) air cooling BTM system at the end of discharge..... | 50 |
| Figure 4.12 Air velocity counter: (a) battery pack side view; (b) Velocity contour from battery pack top view..... | 51 |
| Figure 4.13 Battery temperature vs. time profile for PHP and air cooling at a discharge rate of 1C, at an ambient temperature of 40 °C. | 52 |
| Figure 4.14 Battery ΔT vs. time profile for PHP and liquid cooling at a discharge rate of 1C, at an ambient temperature of 40 °C..... | 53 |
| Figure 4. 15 Model geometry of heat pipe..... | 55 |
| Figure 4. 16 Mass transfer contour with respect to simulation time: (a) t= 0.3 s; (b) t=3s. | 56 |
| Figure 4. 17 Battery temperature vs. time profile for PHP and heat pipes at a discharge rate of 1C, with different ambient conditions. | 57 |

Chapter 5:

| | |
|---|----|
| Figure 5.1 Large Scale Pulsating Heat Pipe Geometry..... | 59 |
| Figure 5. 2 Water distribution at t = 1 s, 12 s. | 60 |
| Figure 5. 3 Steam Distribution at t = 1 s, 10 s. | 61 |
| Figure 5.4 Temperature curve under 1C discharge rate..... | 62 |
| Figure 5.5 Temperature difference comparison on small-scale PHP vs. large-scale PHP. | 62 |
| Figure 5.6 Temperature performance with different cooling methods at 25 °C. | 63 |
| Figure 5.7 Temperature performance with different cooling methods at 40 °C. | 64 |
| Figure 5.8 Battery temperature simulation of 2 C-rate under different systems at 25 °C..... | 65 |
| Figure 5.9 Battery temperature simulation of 2 C-rate under different systems at 40 °C..... | 66 |
| Figure 5.10 Thermal resistance of different fluids for PHPs [27]. | 67 |

Nomenclature

| | |
|----------------|--|
| A | Tube cross-section area, m^2 |
| C-rate | Measurement of a battery is discharged to its maximum capacity |
| D | Diameter, m |
| C_p | Specific heat capacity, $J \ kg^{-1}K^{-1}$ |
| h_c | Convective heat transfer coefficient, $W \ m^{-2}K^{-1}$ |
| I | Applied charge/discharge current, A |
| K | Heat conductivity, $W \ m^{-1}K^{-1}$ |
| L | Length, m |
| L_{eff} | Effective channel length, m |
| l | Thickness of the battery pack, m |
| M | Mass of battery material, Kg |
| \dot{m}_{lv} | Rate of the mass transfer due to evaporation, $Kg / (m^3 s)$ |
| \dot{m}_{vl} | Rate of the mass transfer due to condensation, $Kg / (m^3 s)$ |
| P | Pressure, Pa |
| q_c | Convection heat, J |
| q_r | Radiation heat, J |
| Q_i | Irreversible heat, J |
| Q_r | Reversible heat, J |
| R | Universal gas constant, $8.3143 \ J \ mol^{-1} \ K^{-1}$ |
| R_i | Battery internal resistance, Ω |
| R_e | Reynold number |

| | |
|------------------|--|
| R_{ic} | Internal contact resistance, Ω |
| \overline{R}_t | Average internal resistance of the battery pack, Ω |
| R_{tab} | Battery tab resistance, Ω |
| R_p | Polarization resistance, Ω |
| R_{l-v} | Thermal resistance over liquid to vapor interface, K/W |
| R_{wall} | Thermal resistance through boundary wall conduction, K/W |
| SEI | Solid Electrolyte Interphase |
| T | Temperature, K or $^{\circ}C$ |
| T_{amb} | Ambient temperature, K or $^{\circ}C$ |
| U_{oc} | Open-circuit voltage, V |
| V | Velocity, m/s |
| V | Battery volume, m^3 |
| \vec{V}_v | Vapor phase velocity, S^{-1} |
| x | Distance, m |
| α | Volume fraction, unitless |
| ε_e | Emissivity, unitless |
| ρ | Density of material, Kg/m^3 |
| σ | Stefan-Boltzmann constant, W/m^2K^4 |
| Θ | Angle, $^{\circ}$ |
| τ | Shear stress N/m^2 |
| γ | Surface tension N/m |
| μ | Dynamic viscosity Kg/ms |

Chapter 1: Introduction

1.1 Overview

The electric vehicle industry depends heavily on lithium-ion (Li-ion) batteries for energy storage. Li-ion batteries stand out on the market due to their high energy density, lightweight, and low self-discharge rates. Battery thermal management (BTM) systems are designed to prevent battery thermal runaway from overheating when batteries experience high ambient temperature and high discharge rates. Another critical function of BTM systems is to provide uniform temperature distribution for the battery pack and ensure a proper life cycle from significant capacity fading.

In the past decade, many experiments have been conducted on battery pack heat dissipation and temperature control. For example, a review of heat dissipation performance of a battery pack through forced air by X. M. Xu *et al.* concluded that the horizontal battery pack arrangement improves heat dissipation by shortening the airflow path [1]. The study also investigated the duct placement for battery thermal performance. A well-designed cooling structure with a more miniature flow vortex is essential to optimize temperature control. Other studies employed different water-cooling strategies: sidewall cooling, tap cooling [2], and combined cooling [3] with different inlet mass flow rates to evaluate the temperature control for batteries during the discharge process. Wang *et al.* revealed that sidewall cooling is the most efficient method to guarantee low temperature with fewer design constraints. A passive cooling strategy such as phase change material (PCM) transfers the excess heat from the battery while the material experiences heat conduction to store the extra heat. External air convection is usually required for PCM to promote the efficiency of the system. Thus, additional power consumption is necessary when PCM cooling

is employed. Javani *et al.* [4] conducted a study on battery packs by applying PCM between cells. The results showed that battery temperature is eight degrees lower than the battery under natural convection. Another powerful passive cooling strategy is the heat pipe, which has high thermal conductance to transfers energy without a time delay. The study conducted by Rao *et al.* investigated the heat pipe performance under a small battery pack [5]. The heat pipes evaporation section is placed on the sidewalls of battery packs, and a water sink is placed on the condenser end. The battery temperature difference is 5 °C when the battery is discharged at 35 W. The significant temperature imbalance distribution necessitates a discussion regarding the disadvantage of heat pipes: 1) When steam velocity is higher than surface tension, a large shear force will cause droplet diffusion, which reduces the efficiency of the heat pipe; 2) heat pipes experience dry out when the fluid flow rate is higher than the wick limit, and result accelerated degradation on the heat pipe, 3) with the wick structure inside heat pipes, less space is reversed for the fluid. The boiling limit constrains the heat transfer capacity; thus, heat pipes are restricted to small power devices.

1.2 Objectives

A passive cooling system based on pulsating heat pipes (PHPs) is developed as a BTM system in this thesis. The system is recommended considering the following advantages:

1) Low cost and high flexibility. The working mechanism of PHPs depends on the low pressure, low saturation temperature of the fluid inside the pipe. Unlike the traditional heat pipes, the fabrication cost is reduced since the working mechanism of PHPs does not require a wick structure to perform. In addition, PHPs can bend with multiple turns for design considerations since PHPs do not demand the wick limit for circulation.

2) High fluid density. A low fluid ratio causes the dry out when a traditional heat pipe works under a large power unit. Thus, heat removal of the system is not efficient enough, and degradation of the heat pipe can be accelerated when the heat pipe experiences long-term dry out. For PHPs, the filling ratio can be adjusted from 20-80% of the volume ratio for various scenarios. Therefore, as the fluid ratio increases, PHP's practicality is enhanced for bulk heat sources such as battery packs.

3) High application availability. Standard heat pipe dimensions cannot be modified easily to ensure the efficiency of the heat pipe. For a large battery pack, a heat pipe will be inefficient as a heat conductor since the wicking capacity is reciprocal to pipe length. Meanwhile, the geometry of the heat pipe is usually designed as a circular shape for best performance. A rectangular heat pipe is often needed for space-saving; however, rectangular heat pipes have lower efficiency. For PHP, vapor bubbles and liquid slug are formed within the tube. Pressure differences drive the vapor bubbles to the condenser section. Thus, the application of PHP is more flexible than traditional heat pipes under extensive scale applications. This thesis reveals that PHP provides better performance than active air cooling on a large-scale battery pack for lower maximum pack temperature and more uniform temperature control.

1.3 Thesis Outline

The following text is divided into five main chapters. Chapter 2 provides the technical review on Li-ion batteries, thermal issues during operation and introduces classical BTM systems. Chapter 3 illustrates the mathematical model setup for both battery pack and PHP and discusses the mesh study to define the simulation setup condition. Chapter 4 shows the sensitivity study on PHP and compares the effectiveness of small-scale PHPs to major active cooling systems. Chapter 5 compares the large-scale PHP to air-, liquid-cooling BTM system under both mild and abnormal conditions. Finally, the conclusion of this thesis and some future research topics are presented in Chapter 6.

Chapter 2: Literature Review

A comprehensive understanding of the structure, working principle, and relevant safety issues is essential for studying battery technology. In this chapter, three sections are included to illustrate the battery system. In Section 2.1, Lithium-ion battery classification is discussed. Meanwhile, the structure and working mechanism of the battery are introduced. The relative thermal issue is addressed since thermal runaway is the primary safety consideration for battery packs. Section 2.2 provides a literature review for the developed BTM systems. Performance evaluation of each method and limitation are discussed. Finally, the summary to conclude some remarks are attached in the last section.

2.1 Lithium-ion Battery and the Thermal Issues

The most common Lithium-ion (Li-ion) batteries are LiCoO_2 , LiFePO_4 , and $\text{LiNi}_{x}\text{Co}_{y}\text{Al}_{1-x-y}\text{O}_2$. Fig. 2.1a illustrates LiCoO_2 performance from five perspectives: specific energy, specific power, life span, safety index, and cost. Lithium cobalt batteries are very reactive and therefore suffer from poor thermal stability. The limited availability of cobalt also makes them a more expensive option for use in electric vehicles (EVs) [6]. As Fig. 2.1b demonstrates, LiFePO_4 offers good electrochemical performance with low resistance and provides long cycle life. The phosphate helps stabilize the electrode and offers a higher tolerance to heat, extending the materials' breakdown limit [6]. However, LiFePO_4 has a higher self-discharge than other Li-ion batteries, which causes balancing issues when aging. $\text{LiNi}_{x}\text{Co}_{y}\text{Al}_{1-x-y}\text{O}_2$ has been used by Tesla and other companies due to its high specific energy. The proportion of various metals varies by manufacturer and is a closely guarded formula. Fig. 2.1c shows that combining nickel, cobalt, and aluminum

increases usable discharge capacity and long storage calendar life compared to conventional cobalt-based oxide batteries [7]. However, nickel cobalt aluminum is not as safe as the other batteries listed above, and capacity fading may be severe at an elevated temperature ($\geq 40^{\circ}\text{C}$). As such, a proper thermal management system is needed to monitor pack temperature and protect the battery from overheating.

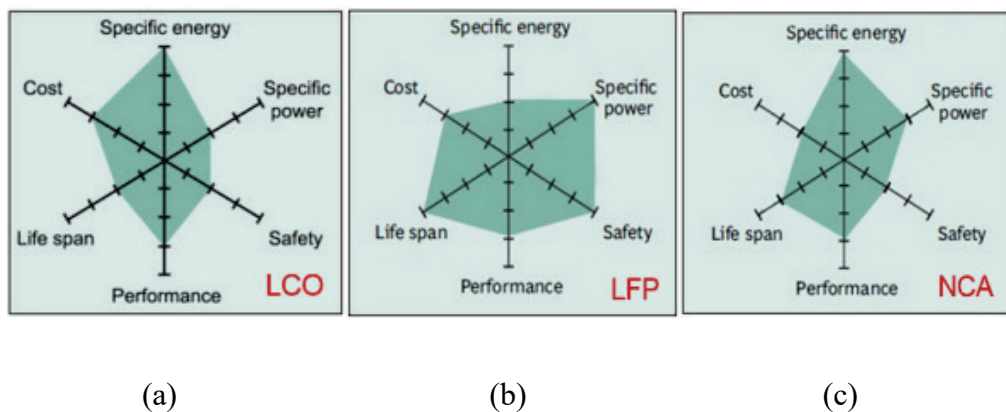


Figure 2.1 Performance of common batteries: (a) LiCoO_2 ; (b) LiFePO_4 ; (c) $\text{LiNi}_x\text{Co}_y\text{Al}_{1-x-y}\text{O}_2$ [5].

The schematic illustrations of a Li-ion battery and its electrochemical reaction are shown in Fig. 2.2. Each reaction cell comprises five components: aluminum current collector, positive electrode (cathode), separator, negative electrode (anode), and copper current collector. While the battery is discharging, lithium ions de-intercalate from the anode, pass the separator to react with electrons flowed through the external circuit, and intercalate into the cathode [8]. Therefore, the discharge capacity is higher when more ions intercalate into the cathode. The reverse reaction takes place during the charging process.

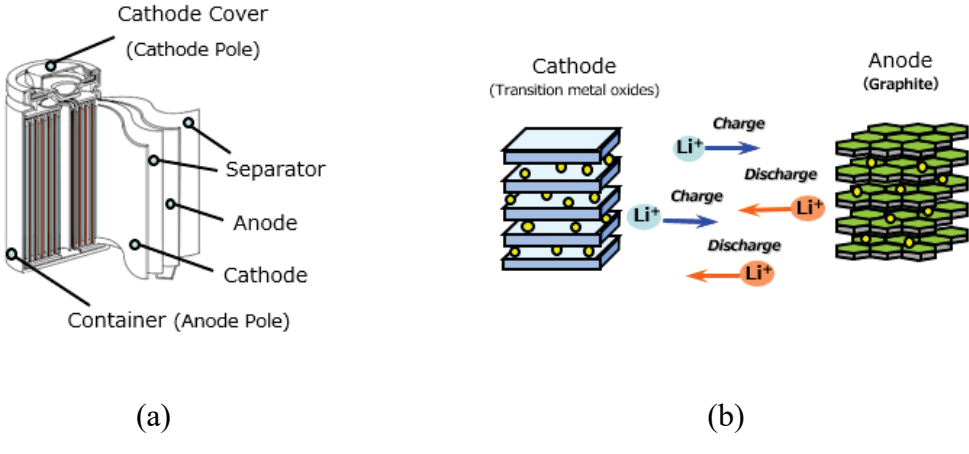


Figure 2.2 (a) Multi-layered core configuration in a lithium-ion battery; **(b)** lithium electrochemical reaction during operation [8].

Under normal operation, lithium ions exchange in cathode and anode to generate the energy needed to supply electrical devices. In this process, the heat generated is mainly divided into irreversible and reversible heat. Irreversible heat is generated due to ohmic potential drop [9]. Reversible heat is produced due to entropy changes of cathode and anode materials during operation. A high internal temperature ($\geq 70^{\circ}\text{C}$) will result solid electrolyte interphase (SEI) film's exothermic decomposition. Negative carbon electrodes may be damaged from side reactions following film decomposition, leading to the production of combustible gas. When the temperature becomes higher ($\geq 150^{\circ}\text{C}$), the positive material will decompose to produce oxygen [11]. The mixture of combustible gas and oxygen will trigger violent reactions. As a result, the battery becomes more flammable, which leads to thermal runaway. The cathode and anode may be in direct contact in abnormal conditions, such as internal short circuits and external short circuits. In such cases, the heat generated includes more than reversible and irreversible heat, and temperature

will soar in a very short time. An effective thermal management system should be developed to avoid the occurrence of thermal runaway, prevent the battery from overheating, and maintain a uniform pack temperature. Section 2.2 provides a brief introduction to BTM systems that have been studied in recent years.

2.2 Battery Thermal Management Systems

This section introduces BTM systems that include active and passive thermal management systems. Relevant studies are provided to elaborate on the working mechanisms and thermal performance of these systems.

2.2.1 Active Thermal Management System

Active thermal management systems are the most commonly applied BTM systems. Active thermal systems utilize the circulation of heat-absorbing material to maintain the system's high efficiency, with air or liquid during the operation as the most common medium. The advantage of this type of thermal management system is that it can control the temperature by adjusting the circulation flow rate in response to real-time conditions [10]. However, active thermal systems consume power and take up space, limiting their usage in real-world applications. This section introduces two types of active cooling systems: liquid cooling and air-cooling systems. Brief descriptions of relevant studies are provided to describe these BTM systems.

2.2.1.1 Liquid Active Cooling System

A liquid cooling system removes heat from the battery pack by liquid circulation. Wang *et al.* proposed a liquid cooling system using thermal silica plates for battery active thermal management systems in EVs. The conceptual design is shown in Fig. 2.3. The battery capacity was 20 Ah in the experiment. Silica-liquid cooling plates (SLCPs) were attached to both sides of the battery. Each SLCP consisted of five copper tubes and two thermal silica plates, which formed a sandwich structure. Each copper tube had an inner diameter of 4 mm with 0.5 mm wall thickness. Inlet velocity was at 0.1 m/s when the battery was discharged at a 3 C-rate. Sensitivity studies on the number of SLCPs, number of copper channels, different inlet flow rates, and different flow directions were included in this work to determine the optimum cooling approach. When the single-side SLCP was applied to the battery, the maximum temperature (T_{\max}) in the battery was reduced by 6 °C compared to the T_{\max} under natural convection. When double-side plates were applied, T_{\max} was reduced by 10 °C. Wang *et al.* revealed that the T_{\max} drop was not linear with respect to the number of channels. Under the 1-channel design, T_{\max} dropped to 48.6 °C, while for 3, 5, 7 channels, T_{\max} was 45 °C, 39.1 °C, and 36.5 °C, respectively. Evidently, battery temperature was kept within the optimum range when the 5-channel design was applied. Overall, the 5-channel design provides better heat transfer performance and isothermal capability than 1 and 3 channels and offers a better trade-off between efficiency and cost than the 7-channel design.

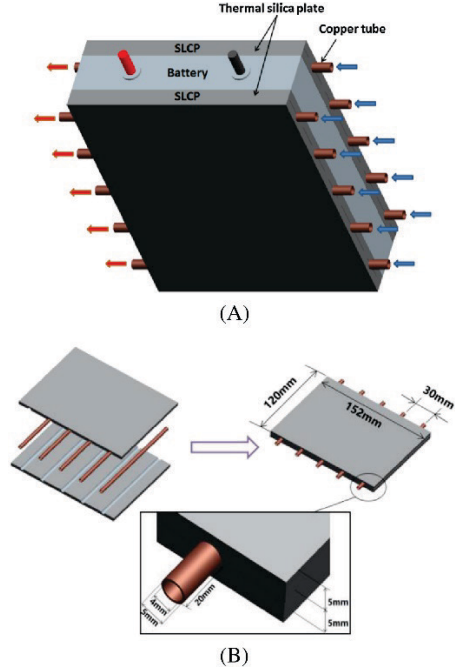


Figure 2.3 (a) Cooling system demonstration; (b) structure and geometry of the silica-liquid cooling plate [12].

The study also investigated the effect of the flow rate. Flow inlet velocity should increase to 0.25 m/s to prevent battery thermal failure when the battery was discharged higher than 3 C-rate [12]. However, when the flow rate exceeded 0.25 m/s, cooling performance was slightly improved. Liquid cooling performance was constrained by the thermal conductivity of the silica plate. Low thermal conductivity can weaken the cooling performance of the system. Another critical factor that affects the BTM performance is the flow direction, which is illustrated in Fig. 2.4. The study showed that the most efficient layout was case 1, which was about 0.6 °C and 1.5 °C lower than cases 2 and 3, respectively. The corresponding temperature nephogram is demonstrated in Fig. 2.5. Case 1 provided lower T_{max} and uniform temperature distribution throughout the experiment.

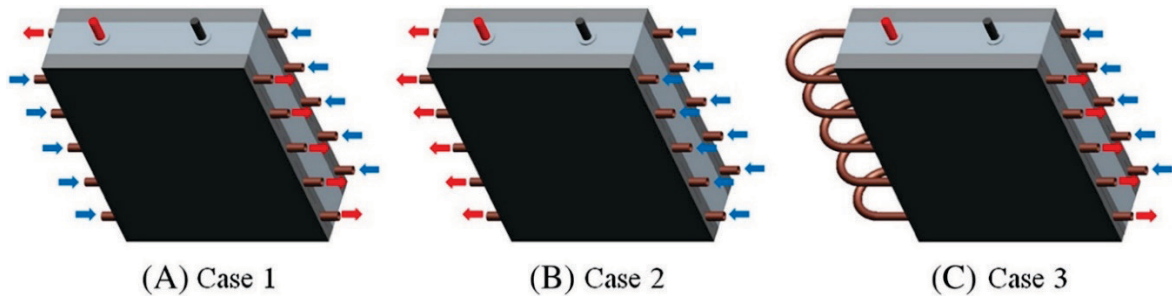


Figure 2.4 Schematic of the cooling system with different flow directions [12].

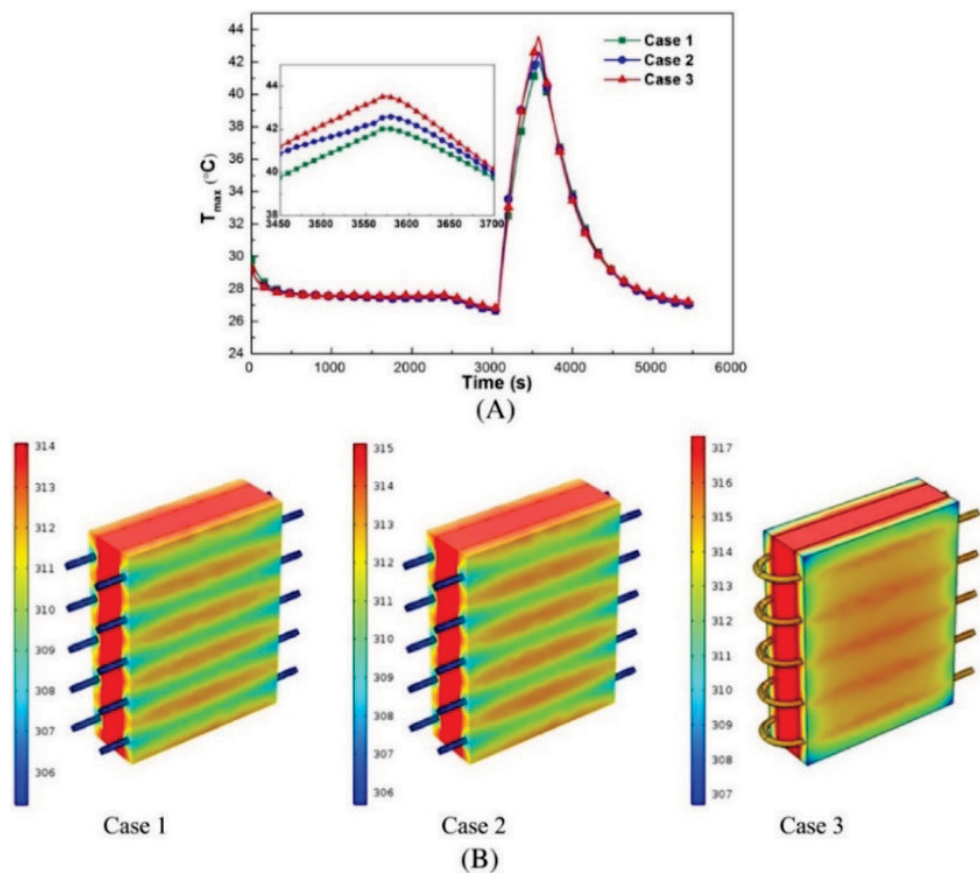


Figure 2.5 Temperature nephograms of the battery at different flow directions [12].

2.2.1.2 Forced Air Cooling System

Forced air cooling is generally achieved by blowing air through the battery pack. The speed of air, location of the air inlet, and cell arrangement are considered critical factors in influencing the turbulence inside the cabin, which in turn affects the system's effectiveness. Wang *et al.* investigated the impact of fan arrangement and battery distance on the effectiveness of a forced-air cooling system. In their study, air inlet velocity was 1 m/s, and the fan radius was 0.03 m with a cross-section area of 0.0028 m². Results showed that the best temperature control layout was the fan placed on top and the air outlet placed at the bottom. The air cabin design is shown in Fig. 2.6. Under this arrangement, the highest temperature difference (ΔT) among cells was 7 °C, and T_{\max} was 38.5 °C for a 3 x 8 battery pack. With the same air-cooling arrangement, for a 5 x 5 battery pack, T_{\max} was 33.58 °C with a lower ΔT (2.95 °C). Thermal characteristics for both battery packs are shown in Fig. 2.7. The study revealed that air cooling performance was highly dependent on the battery layout. Even with one more battery added to the module, the 5 x 5 battery pack achieved better performance due to its symmetrical layout.

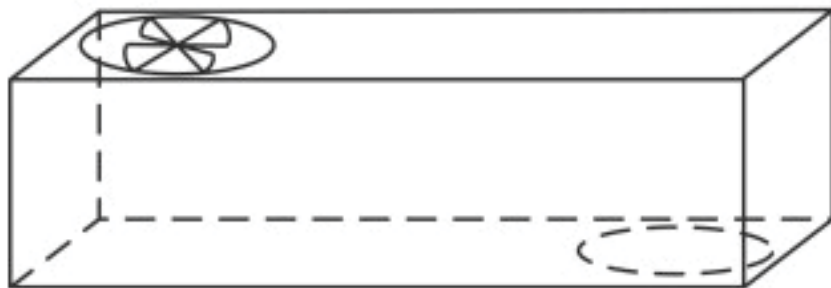


Figure 2.6 Explanation of fan and opening locations [13].

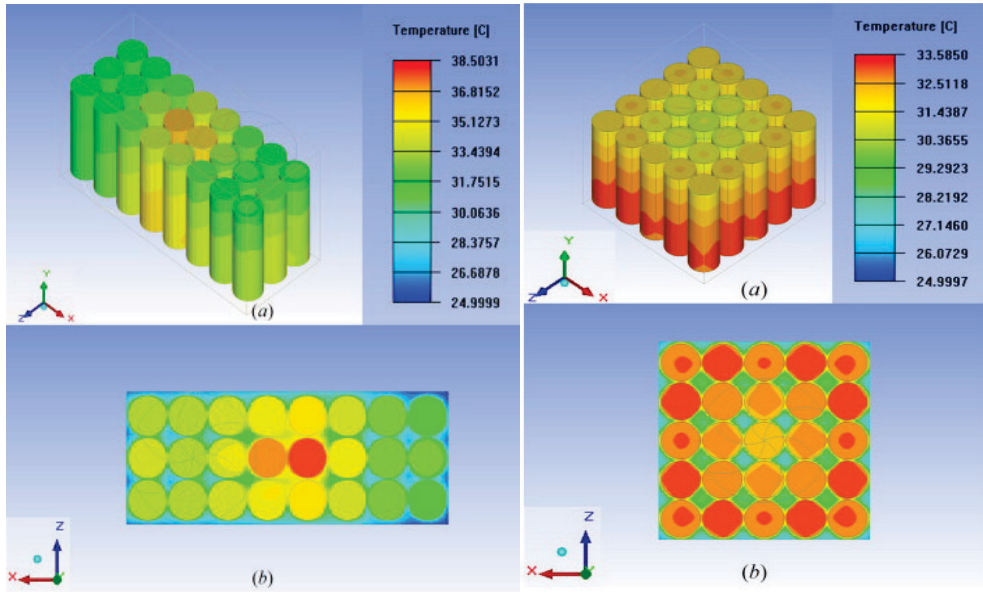


Figure 2.7 Temperature distribution of different battery packs [13].

Wang *et al.* also tested the battery temperature when the inter-cell distances were 0 mm, 0.5 mm, 1 mm, and 2 mm. As shown in Table 1, the study revealed the optimal spacing between cells is 1 mm, as it provides the lowest T_{\max} (33.585°C) and avoids a significant ΔT between cells. The ideal inter-cell distance optimizes cost-saving and space conservation [13].

Table 1. Thermal characteristics of different inter-cell spacing battery modules [13].

| Minimum inter-cell distance (mm) | T_{\max} ($^{\circ}\text{C}$) | ΔT ($^{\circ}\text{C}$) | \bar{T} ($^{\circ}\text{C}$) |
|----------------------------------|-----------------------------------|-----------------------------------|----------------------------------|
| 0 | 35.0807 | 3.5807 | 34.2080 |
| 0.5 | 34.3435 | 3.5039 | 32.9560 |
| 1.0 | 33.5850 | 2.9512 | 32.7560 |
| 2.0 | 34.0112 | 2.7112 | 32.9120 |
| 3.0 | 34.5770 | 3.5770 | 33.2960 |

Sun *et al.* developed a large battery pack cooling model by incorporating a three-dimensional battery pack flow sub-model. Air inlet mass flow rate was set to $0.0283 \text{ m}^3/\text{s}$ with a constant inlet temperature of 29°C . Eighty pouch batteries were applied in the experiment with cooling channels designed in “U-type” and “Z-type” formats; schematic illustrations are shown in Fig. 2.8. The simulation revealed that the “Z-type” flow pattern provided lower surface temperature than the “U-type” model. Moreover, the “Z-type” pattern provided a 43% less pressure drop during the experiment.

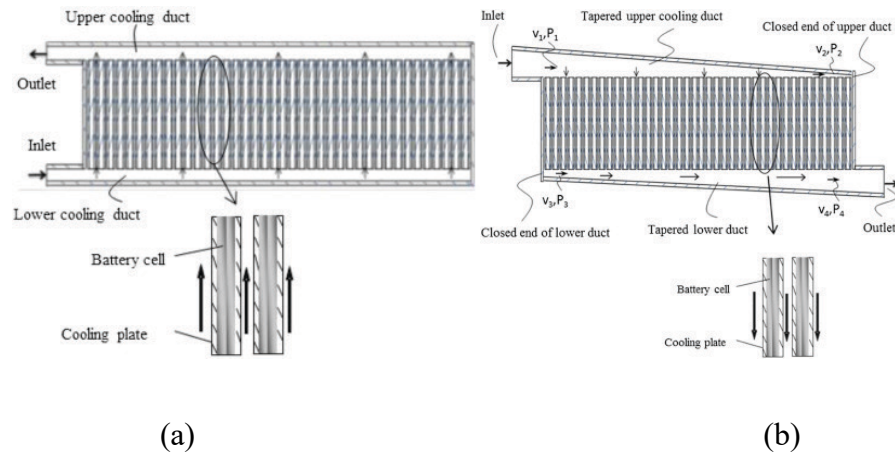


Figure 2.8 (a) Schematic of “U-type” flow battery pack; (b) Schematic of “Z-type” flow battery pack [14].

2.2.2 Passive Thermal Management System

Passive BTM systems are compact, space-saving, and more energy-efficient compared to active thermal management systems. Most passive thermal systems use and maximize natural convection and radiation exchange. The following part introduces two types of passive cooling systems that are commonly researched: phase change material (PCM) cooling system and heat pipe cooling system.

2.2.2.1 Passive Cooling with Heat Pipes

Gan *et al.* investigated the passive thermal management system using heat pipes for cylindrical batteries. The conceptual design is illustrated in Fig. 2.9. In the study, thermal grease was applied between batteries and heat pipes to enhance the contact surface. Heat pipes (sintered copper-water) were 6 mm in outer diameter and 91 mm in length. The condenser section of the heat pipe was flattened to 2 mm thick and inserted into the cooling channel. Smith *et al.* tested the effects of coolant flow rate and inlet coolant temperature.

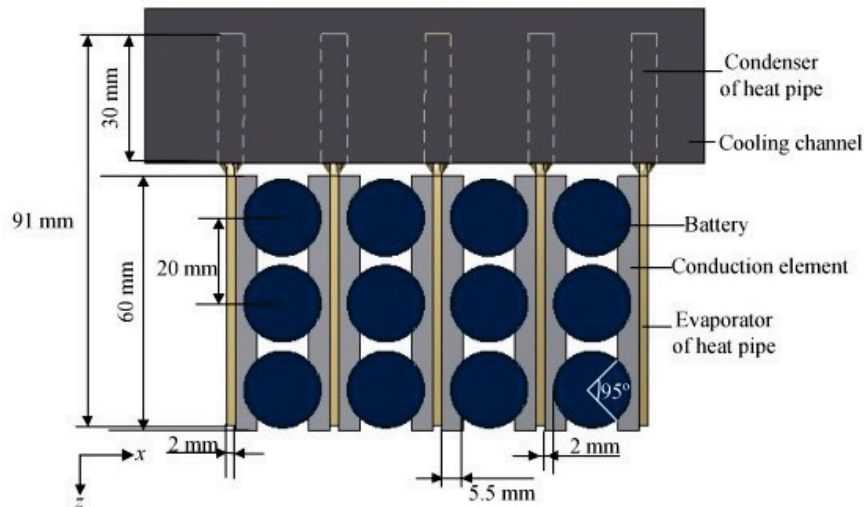


Figure 2.9 Geometry of the battery module and thermal management system [15].

With the installation of heat pipes and inlet flow rate at $1 \text{ L}\cdot\text{min}^{-1}$, battery T_{\max} decreased by $14.03 \text{ }^{\circ}\text{C}$ compared to natural cooling under a 5 C discharge rate. T_{\max} was reduced by $3 \text{ }^{\circ}\text{C}$ when the inlet flow rate was adjusted from $1 \text{ L}\cdot\text{min}^{-1}$ to $3 \text{ L}\cdot\text{min}^{-1}$. The inlet coolant temperature should be controlled between $20 \text{ }^{\circ}\text{C}$ and $30 \text{ }^{\circ}\text{C}$; under this temperature range, batteries are controlled within the acceptable temperature range to prevent failure.

Zhao *et al.* investigated a heat pipe thermal management system based on the wet cooling method. The study utilized the mechanism of mass transfer (water evaporation) to dissipate heat. Two sized battery packs (3 Ah and 8 Ah) were studied, and battery thermal performance was compared to 1) heat pipes inserted in the thermostat bath, 2) heat pipes with fan cooling, and 3) heat pipes placed under natural convection. The illustrations of the experimental setup are shown in Fig. 2.10.

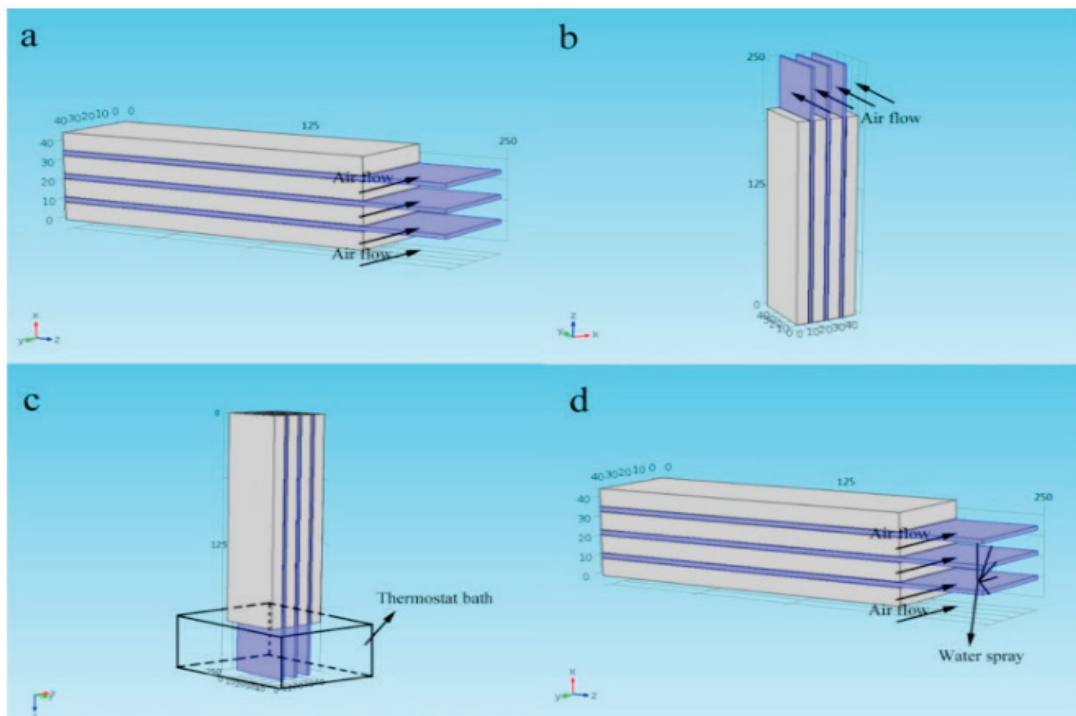


Figure 2.10 Schematic illustrations of four BTM systems: (a) horizontal heat pipes with cooling fan; (b) vertical heat pipes with natural cooling; (c) heat pipes in the thermostat water bath; (d) horizontal heat pipes with wet cooling system [16].

When heat pipes were under natural convection, T_{\max} was 41 °C for the battery pack (3 Ah) discharged under a 3 C-rate; meanwhile, heat pipes under the thermostat bath also experienced a

high temperature increase (37°C). Bubble accumulation at the surface of the heat pipe dramatically decreased heat pipes' thermal conductivity under the thermostat bath strategy. Zhao *et al.* found that wet cooling was the most efficient method as the T_{\max} was 21°C at the end of discharge and wet cooling also provided the lowest ΔT (2°C) among temperature collection points, which was the most efficient BTM system in their study.

2.2.2.2 Phase Change Material Cooling System

Zhao *et al.* researched an internal cooling system based on PCM. PCM was injected into the steel tube to replace the hollow mandrel in the cylindrical battery, and the corresponding setup is shown in Fig. 2.11. This replacement saves space, and the design can effectively alleviate the temperature rise, provide a uniform pack temperature. The experiment was processed under a 4-layer battery pack, and natural convection boundary conditions were applied on the pack's top and bottom surfaces. Noticeably, for a battery pack with higher rows, the effect of convection became negligible, and the battery under external PCM experienced a significant ΔT . Internal PCM provided better performance as a temperature control solution for large battery packs. In addition, internal PCM prevented thermal expansion on battery layers.

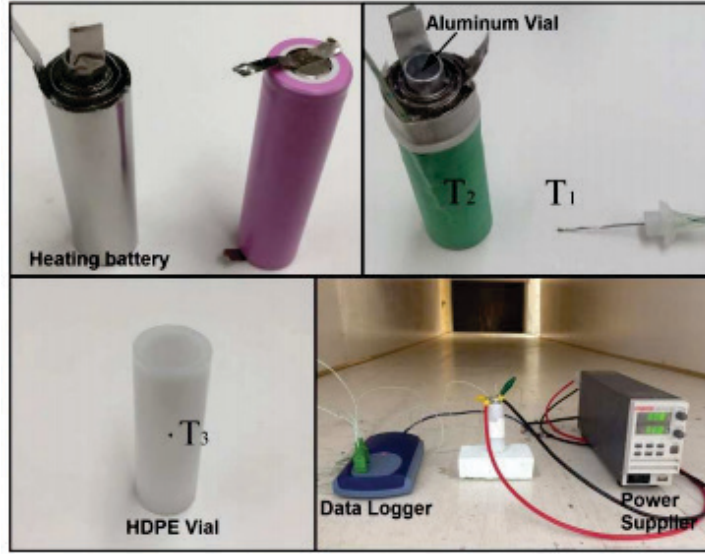


Figure 2.11 Photographs of the thermal test cells and components [17].

Khateeb *et al.* developed an aluminum matrix for a PCM thermal management system to test the improvement of the proposed system. The study compared four cooling systems: PCM alone, PCM with Al-foam, PCM with Al-foam and Al-fins, and natural cooling system. PCM with aluminum fins showed the best overall thermal conductivity through the experiment. The result provided by PCM with Al-foam is the worst, mainly due to the low specific heat capacity of the Al-foam [26]. Overall, the study concluded that the extra heat transfer surface is critical to enhancing PCM performance under battery heat dissipation.

2.3 Summary

The working principle of a Li-ion battery is based on ion intercalation. During the operation, lithium ions migrate between the anode and the cathode via the separator; the semipermeable separator allows the process to be reversible and prevents graphite from flowing into the cathode. The safety issue with Li-ion batteries has triggered many hazards due to excessive heat generated during abnormal operations. Material decomposition inside the battery contains both oxidizer (cathode) and fuel (anode); thus, battery failure may readily result in a fire and lead to thermal runaway [22]. Therefore, to prevent fire and accelerated degradation, batteries should operate within a temperature range that is safe. In the past decade, many BTM systems have been researched. Overall, an optimum BTM system to be applied in EVs should be lightweight, reliable, and easily accessible for maintenance.

BTM systems can be categorized as active BTM systems or passive BTM systems. Active BTM system consumes power to circulate air or liquid to remove heat. A passive cooling system takes advantage of the heat transfer devices, such as the heat pipe with effective thermal conductivity, to dissipate heat without power consumption. Active cooling systems generally perform more efficiently than passive cooling methods in battery pack temperature control; however, due to the power consumption and extra space, battery packs with strict weight and compact design tend to depend more on passive BTM systems.

Chapter 3: Mathematical Modeling and Simulation Setup

In this study, a PHP-based thermal management system was developed. PHPs are modeled via Fluent software simulation. PHPs absorb the heat generated from batteries through thermal conduction and form gas bubbles that oscillate back and forth at a high amplitude. PHPs do not require a porous wick to process a two-phase flow regime, which means they possess the beneficial characteristics of traditional heat pipes, such as the high thermal conductivity, and have low fabrication costs due to their simple structure.

The Fluent modeling setup for the conjugate heat transfer simulation and the governing equations for both batteries and PHPs are illustrated below. A grid independence study was conducted to define the optimal grid size for the simulation. The evaluation of the BTM system was conducted under both standard and abnormal ambient conditions.

3.1 Simulation Setup

In this study, all battery specifications were referenced to LiNiCoAlO₂ batteries. The simulation was realized with eleven battery packs in a parallel connection. Each battery pack was composed of twenty 18650-type batteries, which were connected in series with the voltage cut-off limits of 60 V when discharging. The specifications for a single battery are shown in Table 2. Four BTM systems (small-scale PHP, large-scale PHP, active air cooling, and liquid cooling) were built for cell packs to compare PHP effectiveness. The layout of small- and large-scale PHPs is represented in Fig. 3.1. Liquid cooling follows the same layout as the large-scale PHP, with an inlet velocity of 0.5 m/s. The definitions of standard and abnormal conditions were based on the

ambient temperature. For standard usage conditions, the ambient temperature was set at 25 °C and 40 °C for abnormal conditions.

Table 2. Specification of the LiNi_xCo_yAl_{1-x-y}O₂ battery.

| <i>Battery Specifications</i> | |
|--|--------|
| Width [mm] | 18.5 |
| Height [mm] | 65.3 |
| Weight [g] | 46.5 |
| Nominal Voltage [V] | 3.6 |
| Nominal Capacity [Ah] | 2.9 |
| Specific energy [Wh Kg ⁻¹] | 225 |
| Energy Density [Wh L ⁻¹] | 595 |
| Maximum cut-off charge voltage [V] | 4.2 |
| Minimum cut-off discharge voltage [V] | 2.5 |
| Charge working temperature [°C] | 0-45 |
| Discharge working temperature [°C] | -20-60 |
| Maximum discharge rate [C] | 4.14 |

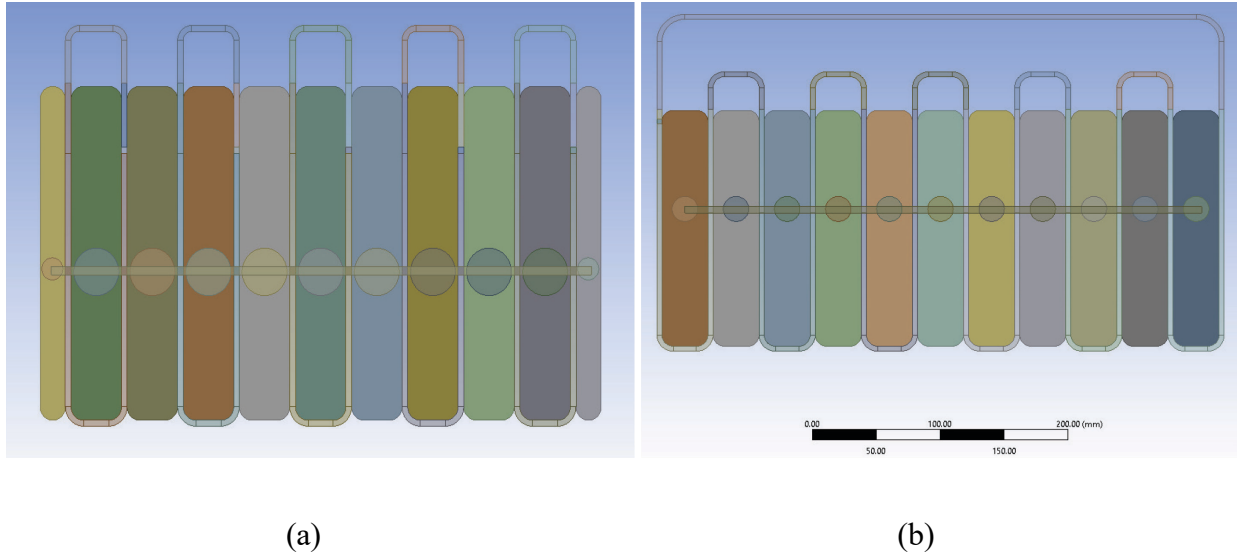


Figure 3.1 PHP thermal management system on 29 Ah battery pack: (a) small-scale PHP; (b) large-scale PHP.

3.2 Thermal Model Setup

During the battery discharge process, heat generated can be categorized as either reversible or irreversible. For a battery model, the reversible heat is due to the entropy change during the reaction [21], which is expressed with the correlation of voltage:

$$Q_r = -IT \frac{dE}{dT} , \quad (1)$$

where E is the open circuit potential of an electrode reaction, I represents the current, and T is the battery temperature.

The irreversible heat is generated by polarizations of the battery tab and internal resistance; thus, the expression is as follows:

$$Q_i = I^2(R_{tab} + R_{ic}) , \quad (2)$$

where the tab and contact resistance are summarized as the average internal resistance of the battery pack, which can be derived by:

$$\overline{R_t} = \sum_{i=1}^n \frac{R_i}{n}, \quad (3)$$

where R_i is the internal resistance of the battery pack at different depths of discharge, which varies from 100 to 400 $m\Omega$ concerning the battery life cycle. R_i is taken as 0.225 Ω for a 18650-type battery with 3 Ah nominal capacity and a 3.7 V nominal voltage [26]. According to Mocek *et al.*, the suggested potential of an electrode reaction is 0.86 mV/K for a ternary Li-ion battery [23]. The battery's reversible heat is negligible compared to the energy caused by internal resistance from the literature reference. Based on the brief calculation from Mocek *et al.*, internal resistance could cause ten times the heat generated by electrode reactions.

The energy balance of the battery pack is represented with respect to the specific heat of the material and the density of the battery cell. The energy balance of the battery remains the same when no cooling strategy is applied:

$$q = MC_p \frac{dT}{dt} = V\rho C_p \frac{dT}{dt}, \quad (4)$$

where M is the mass of the battery, and C_p is the specific heat of each component. The calculation of specific heat depends on the average values of the heat capacity. The thickness of each component and the thickness of the entire battery are considered. Defining the specific parameters is essential to guarantee that the simulation is accurate to real-world applications. An experiment by Inforlab was conducted to determine the specific heat under different operating temperatures from 25 to 55 $^{\circ}\text{C}$, and the results are given in Table 3 [18]. The average value of specific heat is 832 $\text{J kg}^{-1} \text{ K}^{-1}$. According to the 18650-type battery specifications, a single battery weighs 0.0465

kg with a volume of 0.00001275 m^3 . The density is 3764.7 kg/m^3 . For a single battery, a 1°C elevation generates 38.7 J. To validate the result, Zhang *et al.* calculated ρC_p as $2421(\text{kJ}/\text{m}^3 \text{ K})$ and concluded that the energy generated by the battery is $31 (\text{J/K})$ [20].

Table 3. Battery specific heat concerning temperature [14].

| Temperature, T ($^\circ\text{C}$) | Specific Heat Capacity, $C_p(\text{J/gK})$ |
|-------------------------------------|--|
| 30 | 0.85 |
| 35 | 0.82 |
| 40 | 0.84 |
| 45 | 0.81 |
| 50 | 0.84 |

In a battery cell, the transient 3-dimensional energy balance equation is as follows:

$$\rho C_p \frac{dT}{dt} = Q + K\Delta T , \quad (5)$$

where the left side term is the heat stored/generated in the battery, q is the heat generation within the battery (reversible and irreversible). Convection q_c and radiation q_r are considered as the battery boundaries

$$q_c = h_c(T - T_{amb}) , \quad (6)$$

$$q_r = \epsilon_e \sigma (T^4 - T_{amb}^4) , \quad (7)$$

Eqs. (6) and (7) can be further combined as:

$$K \frac{dT}{dl} = h_c(T_{amb} - T) + \epsilon_e \sigma (T_{amb}^4 - T^4) , \quad (8)$$

where h_c , ϵ_e and σ denote the convective heat transfer coefficient (set at $10 \text{ W m}^{-2} \text{ K}^{-1}$ for natural convection), emissivity, and Stefan-Boltzmann constant.

To properly evaluate total heat transfer in a PHP, the radial heat transfer between copper wall and working fluid, evaporative heat transfer, and the condensation heat transfer should all be considered, where the expression is listed below in an analogy of thermal resistance:

$$Q = \frac{\Delta T}{2R_{wall} + R_{evap} + R_{cnod} + R_{l-v}} = \frac{\Delta T}{\frac{L_{eff}}{K_{eff} A_{cross}}} , \quad (9)$$

where inside the PHP, both sensible and latent portions exist. Sensible heat transfer to liquid slug as the temperature increases to enter evaporator section, and when slug moves back to condensation section, it gives up heat. Latent heat transfer generates the pressure differences that drive the flow to oscillates.

The heat transfer phenomena in PHP can be evaluated by solving mass, momentum, and energy conservation equations for the liquid slug and vapor plugs. The equation of momentum applied to the entire liquid slug is shown [19]:

$$AL_p \rho_L \frac{d^2x}{dt^2} = [(p_{l1} - p_{l2})]A - 2p_l g A x - \pi D \tau_1 , \quad (10)$$

where A is the cross-sectional area of PHP. The pressure difference between a liquid slug and the interfacial tension is defined as follows:

$$p_{l1} - p_{l2} = (p_{v1} - p_{v2}) - \frac{2}{r} (\gamma \cos \theta_1 - \gamma \cos \theta_2) . \quad (11)$$

Calculate the velocity, and considering the friction between the liquid slug and pipe wall, the shear stress can be found as follows:

$$V_1 = \frac{d_x}{d_t}, \quad (12)$$

$$\tau_1 = \frac{1}{2} C_1 \rho_1 V_1^2, \quad (13)$$

$$R_e = \frac{\rho_1 V_1 D}{\mu_1}, \quad (14)$$

| Value of C_1 | |
|-----------------|---------------------|
| $R_e \leq 1180$ | $16/R_e$ |
| $R_e > 1180$ | $0.0078 R_e^{-0.2}$ |

After the consideration of momentum, the most critical mechanistic model behind PHP is the evaporation and condensation mass transfer, which is applied by the Lee model behind Fluent. Inside the Lee mode, the liquid-vapor mass transfer is illustrated by the vapor transport equation:

$$\frac{d}{dt}(\alpha_v \rho_v) + \nabla \cdot (\alpha_v \rho_v \vec{V}_v) = \dot{m}_{lv} - \dot{m}_{vl}, \quad (15)$$

where ANSYS Fluent defines positive mass transfer as being from the liquid to vapor for evaporation problems, based on the following temperature regime, the mass transfer can be described as in Table 4. The value β_1 of and β_2 should theoretically be different, and the theoretical value is based on few strong assumptions such as flat interface, a dispersed regime with constant diameter. The bubble diameter and accommodation coefficient to derive the value of β_1, β_2 are usually not very well known, and by default, the coefficient would be set as 0.1.

Table 4. Formulas of $S_{m,l}$ and $S_{m,v}$.

| Formula | $T \geq T_{sat}$ | $T < T_{sat}$ |
|-----------|--|--|
| $S_{m,l}$ | $\beta_1 \alpha_l \rho_l \left \frac{T - T_{sat}}{T_{sat}} \right $ | $\beta_2 \alpha_v \rho_v \left \frac{T - T_{sat}}{T_{sat}} \right $ |
| $S_{m,v}$ | $\beta_1 \alpha_l \rho_l \left \frac{T - T_{sat}}{T_{sat}} \right $ | $\beta_2 \alpha_v \rho_v \left \frac{T - T_{sat}}{T_{sat}} \right $ |

One more consideration is the size of PHP during the design process. Santhi *et al.* [26] suggested the critical diameter of the PHP, which can be taken as a reference to validate the simulation value:

$$D_{min} = 0.7 \sqrt{\frac{\gamma}{(\rho_l - \rho_v)g}} \quad (16)$$

$$D_{max} = 2 \sqrt{\frac{\gamma}{(\rho_l - \rho_v)g}} , \quad (17)$$

where γ is the surface tension of the liquid, which is taken as 0.072 N/m for water and 0.054 N/m for ethanol, and the maximum diameter is calculated for water is 4.98 mm, and for ethanol and methanol is 3.4 mm. The other consideration is the filling ratio of the PHP, which the maximum filling ratio should be controlled under 80% to prevent the PHP works as a single-phase thermosyphon [37]. The maximum feasible filling ratio is validated via the Fluent simulation to provide a compact design of the PHP-based BTM system.

3.3 Grid Independence Study

The importance of the grid independence study was to eliminate the influence of the grid size on the computational results. With the non-linearity of the governing equations and different geometry scales, the simulation process is very time-consuming. It is critical to find an optimal grid size that allows the solution to be converged and also reduces simulation time. A 0.5 m cylinder pipe with a 0.05 m diameter was computed to process the independent study, with an inlet velocity of 0.001 m/s. The element size was initially defined as 25 mm on the cylinder outlet. The number of divisions on the size edge was initially chosen as 20 and increased to 10 more divisions with every set of simulations. In the simulation, the outlet was defined as outflow, with a ratio of one. The outlet velocity parameter and maximum velocity were created as output and stored as an MSC file. Fig. 3.2 depicts the results for the grid independence study with respect to outlet velocity; it is difficult to observe the optimal grid size due to rapid variation in the average velocity plot. Thus, other parameters should be evaluated to determine the appropriate mesh sizing.

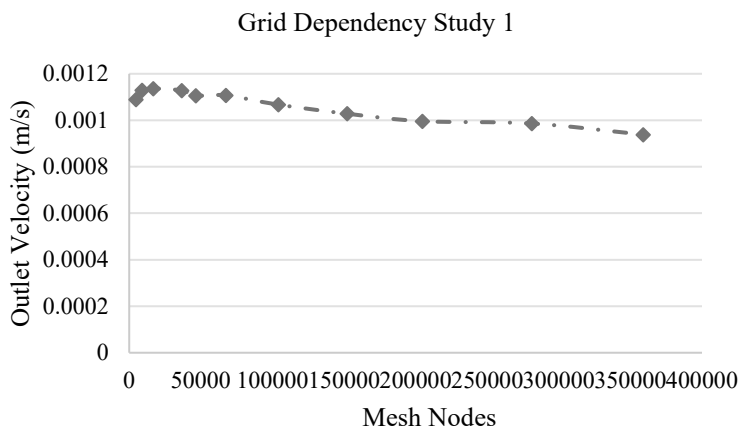


Figure 3.2 Grid dependency test by the average velocity.

Fig. 3.3 demonstrates the grid size correlation with respect to the maximum outlet velocity. In the maximum velocity plot, the variation is significant with respect to mesh. The maximum outlet velocity is stable after the cell size increases beyond 67620 (mesh size 0.5 mm). The marked point in the plot is considered the optimal mesh size for the calculation since there is less convergence time and the result is precise compared to smaller mesh size.

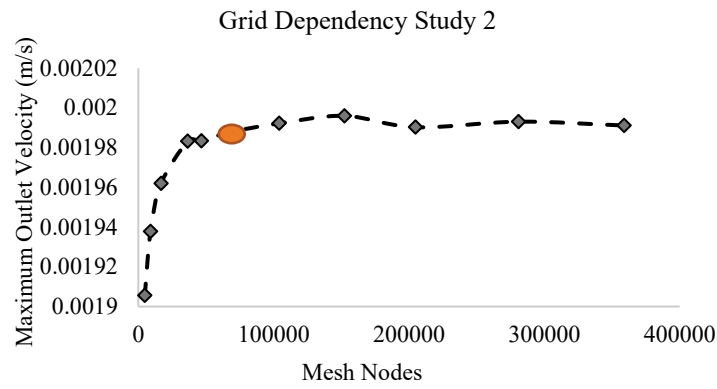


Figure 3.3 Grid dependency test by maximum velocity.

In the mesh generator, hexahedron is generated for both small- and large-scale PHP and accepted due to the high orthogonal quality. As the solution accuracy in hexahedral meshes is usually the highest among others. The small section of the meshed PHP, battery, air cooling channel, and water cooling is shown in Fig 3.4.

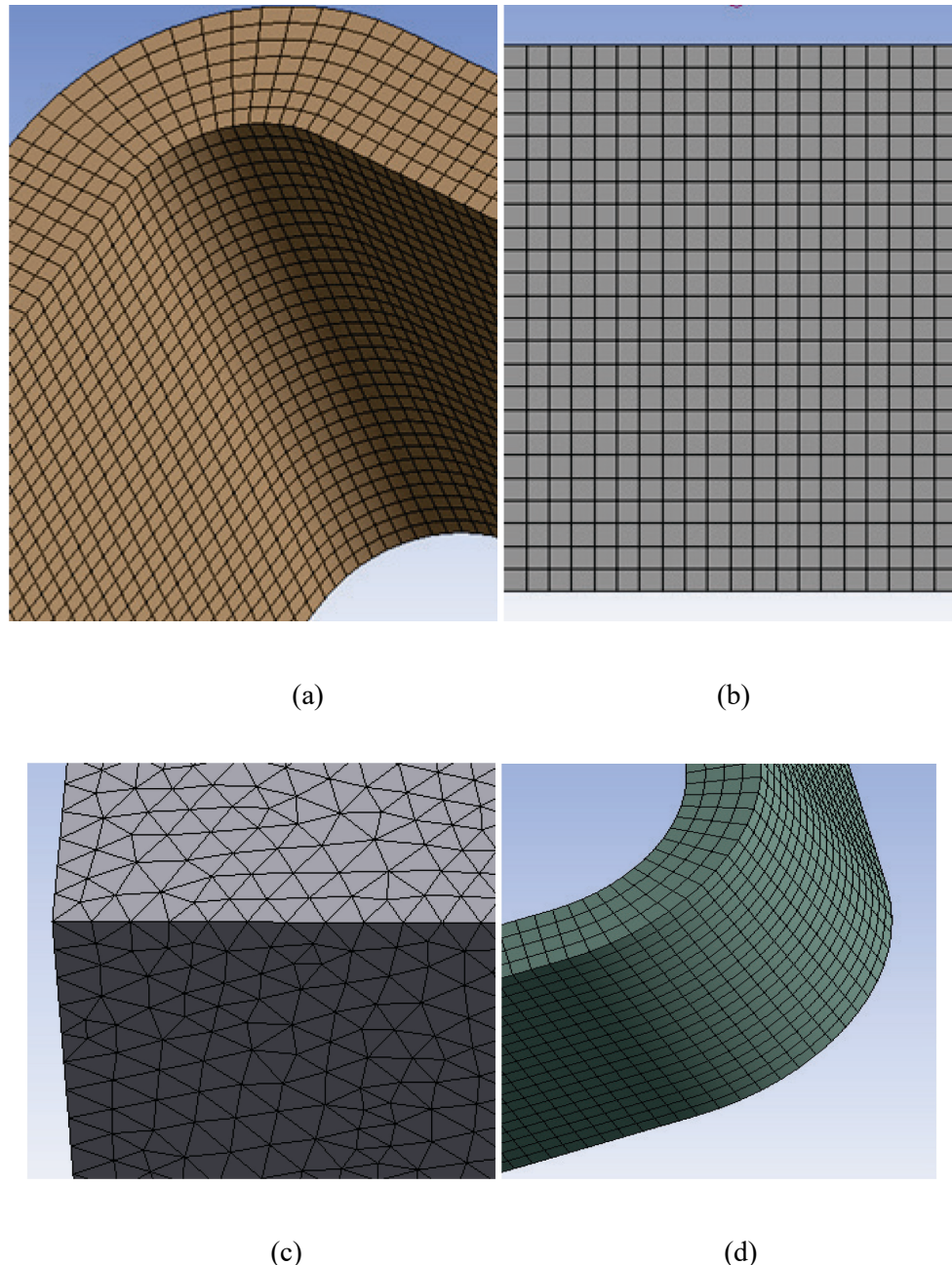


Figure 3. 4 A small section plan view of: (a)PHP meshed in Fluent; (b) battery meshed in Fluent; (c) air cooling meshed in Fluent; (d) water cooling channel meshed in Fluent.

T_{\max} is applied to validate the grid independence on the forced air-cooling model. The test results are shown in Fig. 3.5; when node varies from 13606389 to 26217884, the results differ from 0.513%. In order to validate the accuracy of simulation, a study by Wang *et al.* observed a

similar temperature control behavior on a battery pack with the exact air duct placement during the experiment [13]. The correlation of grid size, mesh quality, skewness is shown in Table 5. Thus, the element size was applied as 0.5 mm, and Computational Fluid Dynamics (CFD) was checked as a physics preference. The maximum skewness was 0.137, with the lowest orthogonal quality of 0.83422. The generate mesh is ready for the Fluent setup as the orthogonal quality and skewness were acceptable.

Table 5. Mesh quality study

| Element size (m) | 0.026 | 0.005 | 0.0008 | 0.0005 |
|--------------------|---------|---------|---------|-----------|
| Nodes | 237,003 | 273,781 | 568,037 | 2,223,745 |
| Orthogonal Quality | 0.58432 | 0.63768 | 0.7331 | 0.83422 |
| Skewness | 0.63136 | 0.5311 | 0.39852 | 0.13731 |

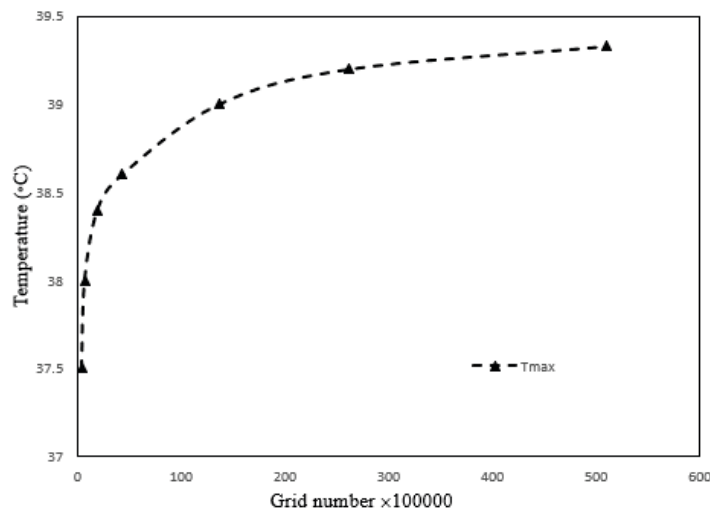


Figure 3.5 Grid independency test on the battery pack.

3.4 Fluent Modeling

The working mechanics of a PHP is to operate under a near-vacuum condition inside the pipe, but have air is reserved as the primary material. Air is needed as the starting condition; if only water and water vapor are added, the simulation starts as the water vapor is already formed inside the pipe. In this case, mass transfer cannot be defined. For the multiphase selection, volume of fluid (VOF) was checked for three phases: air, water, and steam. Implicit body force was also checked; the phases are defined in Table 6. For the multiphase physics, water and water vapor were listed under the phase change as evaporation and condensation. The working temperature of evaporation was set at 30 °C since the pressure inside a PHP was set to 4 kPa. Both wall adhesion and surface tension were activated in the VOF model. Surface tension for three phases was 0.072 N/m, as referred from the textbook [25]. For the viscous model, K-epsilon was applied with “enhanced wall treatment,” as the model can predict far from the boundary wall [27].

Table 6. Description of the phases

| Phases | Fluid |
|--------------------|--------------|
| 1- Primary phase | Water vapor |
| 2- Secondary phase | Water liquid |
| 3- Secondary phase | Air |

Table 7. Details of numerical simulation.

| Items | Content | Items | Content |
|------------------|--------------|----------------------------|--------------|
| Model | 3D Transient | Pressure-velocity coupling | Coupled |
| Multiphase model | VOF Explicit | Pressure interpolation | PRESTO |
| Surface Tension | 0.072 N/m | Momentum and energy | Second-order |
| Viscous model | K-epsilon | Contact angle | 21° |

For the battery model inside the Fluent setup, the command “define models addon-module” was used to dispatch the battery model. Inside the battery model setup, battery specification was set from Table 2. Both active zone (cells) and passive zone (tabs and busbars) were taken as the heat source. For the model parameter section, the reference capacity was written the same as the nominal power. The command “rpsetavr battery/max-n-parallel-per-stage 20” was applied to doubling the number of allowable connections since the default parallel number of connections was less than 10. “Print Battery System Connection Information” should check every time; this is listed under the electric contacts section and was used to verify that the battery connection was correctly set up. Finally, a transient battery model was generated, which is shown in Fig. 3.6; however, battery packs required initialization for further simulation.

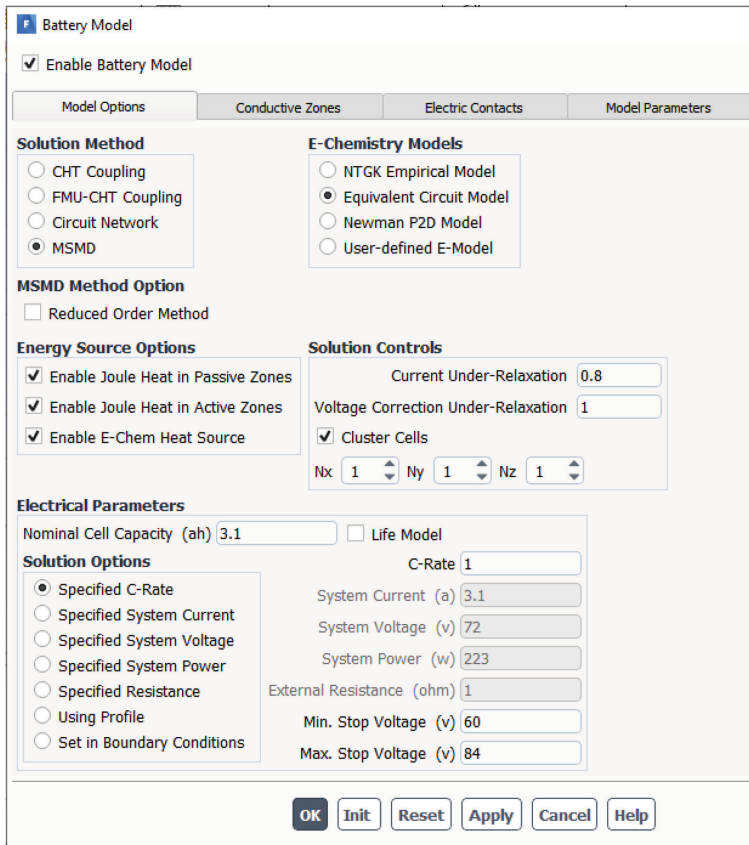


Figure 3. 6 Fluent battery model setup

Materials. Air, water liquid, and water vapor were selected for PHP with default parameters.

In Fluent material setup, the battery material was created and named “e_material,” which includes the battery’s specific energy, density, thermal conductivity, and electrical conductivity. The derivation of these parameters is listed in section 3.2. Copper was selected from the database for all tabs and busbars.

Cell zone conditions. All materials needed to be defined under this section, and the operating condition remained unchanged. The heat source term for battery cells and tabs was enabled with “msmd battery mode”. As the VOF model was activated for PHPs, all fluid domain was shown as the mixture.

Boundary conditions. Two different parts needed to be set for PHPs. The condenser section of the pipe was accompanied by a constant wall temperature of 28 °C with a specific wall thickness of 1 mm. For the evaporator section that contact with the battery, the ambient temperature was set concerning testing conditions, and the shell conduction should be checked with the same wall thickness of 1 mm. The heat generated by batteries was transferred axially to PHPs. After the initialization, the battery temperature was set to the desired ambient temperature of 25 °C (standard ambient condition) and 40 °C (abnormal ambient condition). One more consideration is the contact angle when wall adhesion is applied under the volume of fluid model. The static Contact angle is assumed as the surface normal in cells near the wall, which is known as the dynamic boundary condition. According to Shekhawat that the static contact angle is set as 21 for all walls [38]. Relaxation factors were kept to default values, as shown in Table 6. The transient simulation was started once the step size and number of steps are defined.

Table 8. Relaxation factors.

| Pressure | Density | Energy | Momentum | Turbulent dissipation rate | Body Force |
|----------|---------|--------|----------|----------------------------|------------|
| 0.3 | 1 | 1 | 0.7 | 0.8 | 1 |

Running the simulations. The biggest issue with the simulation of multiphase flow is that the time step needs to be sufficiently small to capture the movement of the particles. Under transient simulation, a large time step would diverge very quickly to fail the simulation; thus, the demonstration of bubble movement cannot be captured. The purpose of transient state simulation

is to observe the liquid plug and vapor bubbles inside the PHP. Different time steps are used, and the main issues are summarized in Table 8. In the end, a time step of 1×10^{-5} was the best choice since all the others were diverging during the simulation. Furthermore, the number of steps was chosen to have 15 seconds of simulation. For conjugate heat transfer simulation, the selection of time step has much less restriction since the convergence condition is not applied to the conjugate heat transfer simulation.

Table 9. Issues for different time steps

| Time step (s) | Issue |
|---------------|--|
| 0.1 | Diverges very fast |
| 0.01 | Diverges very fast |
| 0.001 | Diverges |
| 0.0001 | Diverges after some time |
| 0.00001 | Takes a long time but does not diverge |

The computational time was around 20 hours, using a computer with 6 cores. The approach is not the best one; however, the results seem adequate as expected: water sticks to the walls, liquid columns are formed, and fluid is observed to oscillate. The following images in Fig. 3.7 are the synthesis of the results in water VOF. The evaporation section is set at $80\text{ }^{\circ}\text{C}$, and condensation is set at $23\text{ }^{\circ}\text{C}$ to observe the two-phase flow. This setup is only used to validate the model under transient heat transfer. In the conjugate heat transfer, bubble formation would be delayed due to the axial conduction by battery packs. During the transient simulation, the fluid fraction is observed as 1 in the evaporation section, and the volume fraction became less with the increment

of time steps. The change of fluid volume fraction verified the working mechanism of the developed PHP system.

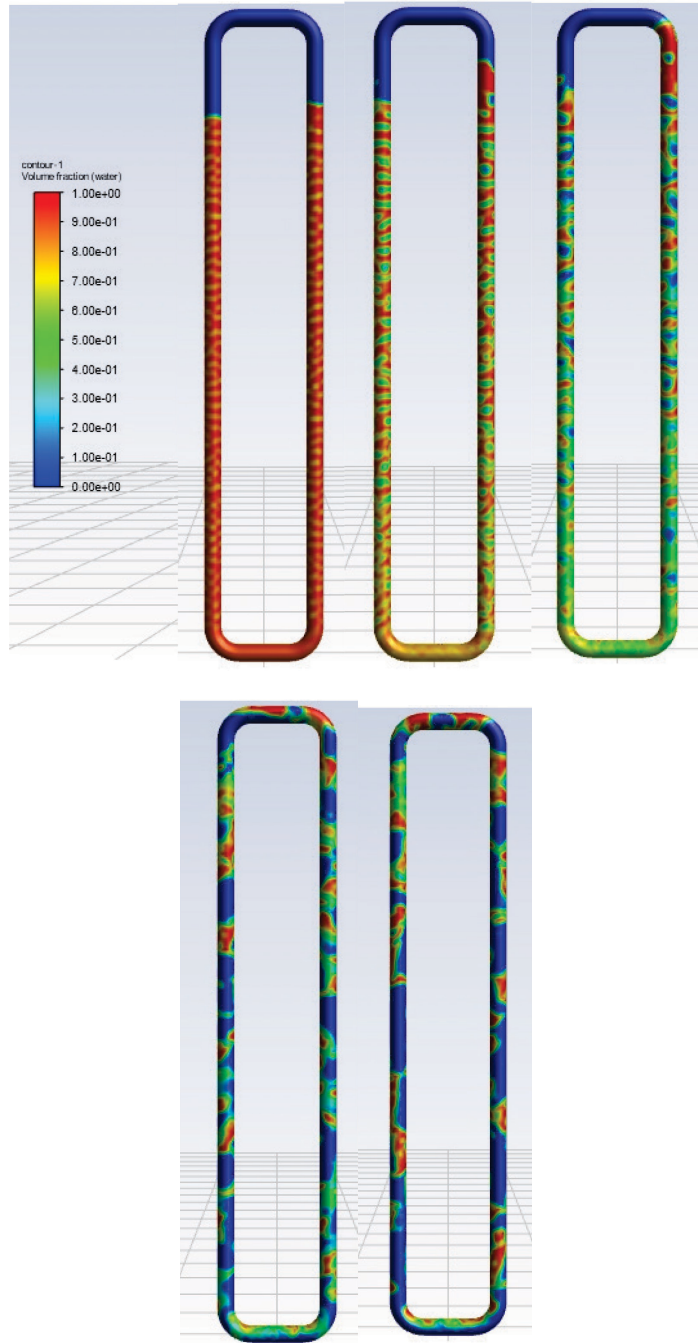


Figure 3.7 Liquid distribution at $t = 1\text{ s}, 3\text{ s}, 5\text{ s}, 8\text{s}, 10\text{ s}$, respectively.

Chapter 4: The Evaluation of Pulsating Heat Pipe Cooling

Performance on Li-ion Battery

The importance of the BTM systems has been previously shown in other studies; however, the application of PHPs for a large battery pack is rarely mentioned and investigated. The primary goal of this thesis is to optimize the size of the PHP. The sensitivity study evaluated the impact of wall thickness, condenser length on the performance of the battery cell. Wall thickness of 0.5 mm and 1 mm, different condenser lengths (10 mm, 15 mm, and 20 mm) were tested to determine optimal PHP parameters under different usage conditions. The effectiveness of the designed PHP-based system was compared to active air cooling, liquid cooling, and traditional heat pipes under different operating conditions.

4.1 Pulsating Heat Pipe Sensitivity Study

Dimensional factors are considered to be critical factors in affecting PHP performance. The sensitivity study evaluated the optimal wall thickness and condenser length to conclude PHPs with the best trade-off between performance and volume ratio. The optimal parameters were applied for further comparison of BTM systems.

4.1.1 Effect of Wall Thickness

The PHP simulation was constructed with 4 mm in width, and the wall thickness is set at 0.5 mm and 1 mm, respectively. Inner pipe diameter changed the heat transfer area, which might affect the performance of heat dissipation. Previous experiments have used a wall thickness of 1 mm; however, a thinner wall thickness has not been applied to validate the performance. For PHPs,

the acceptable range for the inner diameter is between 1.9 mm and 5.4 mm [20]. For the 1C discharge rate, Fig. 4.1 shows that 1 mm wall thickness has a slightly higher heat removal rate. One millimeter wall thickness brought T_{max} to 1 °C lower than the T_{max} under 0.5 mm wall thickness. Thermal resistance (°C/W) was increased with higher wall thickness, which prevented bubble accumulation at the boundary wall, thereby enhanced thermal performance. Under high ambient temperature, thermal characteristics by different wall thicknesses remained relatively similar. Although slight variations were apparent, the overall performance was still favorable. One millimeter wall thickness provided lower battery T_{max} (48 °C), and when PHP wall thickness was reduced to 0.5 mm, T_{max} was 49.5 °C, which the temperature is just under the pass criteria (50 °C).

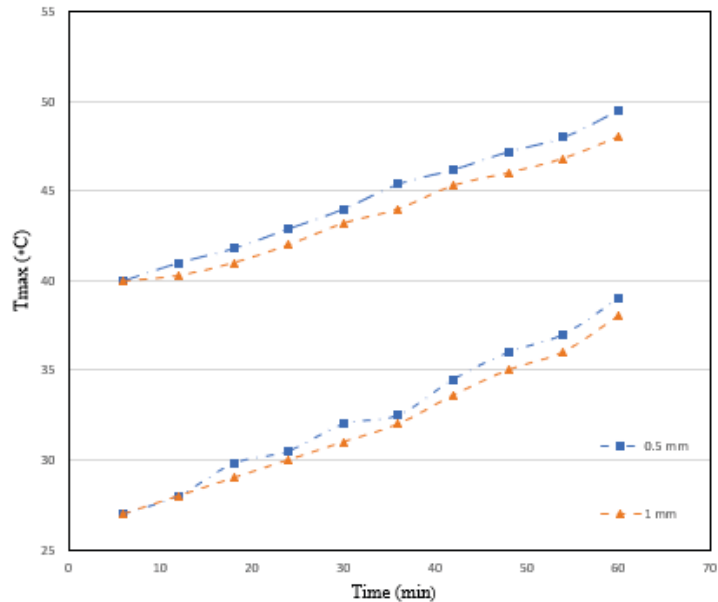


Figure 4.1 Battery temperature by different wall thickness at different ambient conditions.

Fig. 4.2 shows the battery pack ΔT during the discharge. When wall thickness increased to 1 mm, battery ΔT was reduced slightly (by 0.15 °C). The ΔT change was significant under abnormal

conditions. The high ambient temperature may account for the higher ΔT ; as battery materials are highly active to high temperature, reactions become faster under this scenario. However, the T_{\max} comparison through different wall thicknesses was negligible compared to the total temperature rise (3% variation). Consistent with these findings, Ahmed *et al.* conducted a sensitivity study to validate the simulation result and found that conduction heat transfer through the wall did not change significantly as a function of wall thickness [30].

The study revealed by Ahmed *et al.* is attached in Fig. 4.3, which verified the effect of wall diameter remains negligible for the conduction heat transfer. In conclusion, the change of wall thickness is negligible compared to the total temperature rise at the end of discharge. A wall thickness of 1 mm is recommended as the performance was slightly improved due to lower wall temperature to enhance better slug circulation under these conditions. Moreover, from a manufacturing perspective, a higher wall thickness is easy to achieve and more desirable to guarantee the modulus of rigidity.

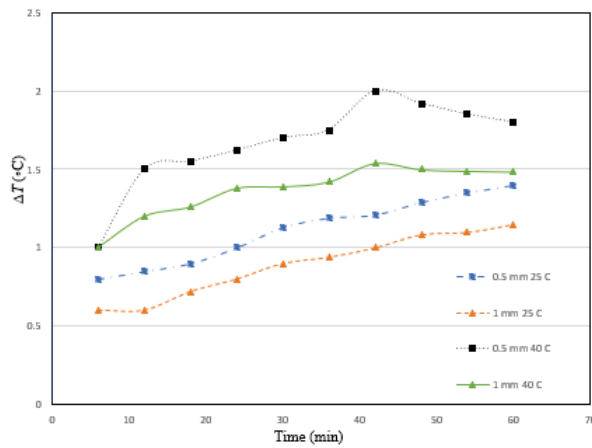


Figure 4.2 Temperature difference with respect to the wall thickness at different ambient conditions.

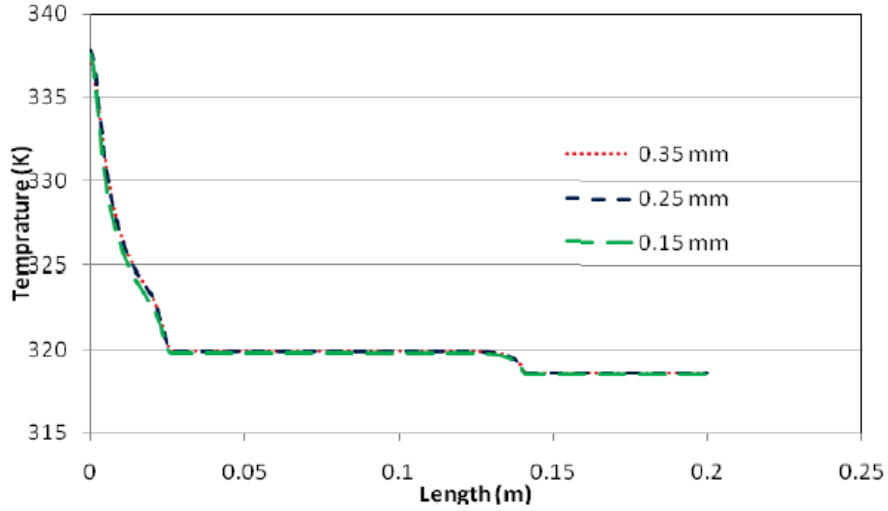


Figure 4.3 Wall temperature against different wall diameters [30].

4.1.2 Effect of Condensation Length

The study of condensation length of a PHP on battery temperature control was conducted with a 1C discharge rate under different ambient conditions to guarantee effective performance. The minimum feasible condensation length was obtained via Fluent simulation.

The wall thickness was set to 1 mm based on the previous simulation. A condenser length of 20 mm was applied initially for the heat pipe with a 7 mm arc length of the pipe, which controlled the battery T_{max} at 39 °C. The PHP has a condenser length of 20 mm; the filling ratio was 75.5%, which is just below the maximum suggested filling ratio (80%). Generally, the PHP works as a true pulsating device when the fill ratio is between 20% to 80%. However, the exact range differs for different working fluids and different constructions. The filling ratio is generally chosen between 60% to 80%, and the performance of different filling ratios is illustrated in Fig. 4.4 [39]. Increasing the condenser length could improve performance as the filling ratio decreases; however, the purpose of this sensitivity study was to find the minimum feasible length.

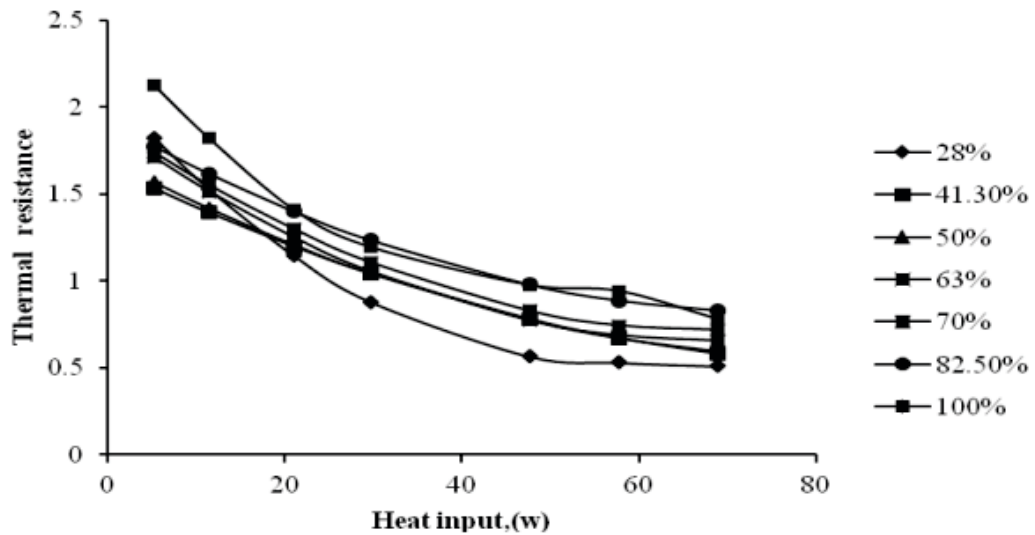


Figure 4.4 Variation of thermal resistance with heat input [39].

During the experiment, the condenser length was sequentially reduced by 5 mm to observe the PHP performance; meanwhile, the battery pass criteria were set to 50 °C and 55°C for different ambient conditions. Fig. 4.5 illustrates the temperature curve under different condenser lengths. Based on the findings, the recommended minimum condenser length is 15 mm at mild ambient conditions, with the battery T_{max} at 45 °C with a temperature elevation of 20 °C. The temperature rise was acceptable but not favorable compared to the 20 mm condenser length (T_{max} of 39 °C). Pack temperature elevation is enlarged under abnormal ambient conditions. Both 10- and 15-mm condenser lengths did not effectively control the battery temperature; the battery T_{max} reached 57 °C and 60 °C, respectively. When the condenser length is set at 20 mm, the temperature was well controlled to 48 °C, which the pack temperature elevation is only 8-degree. Once the filling ratio is over 80%, the mechanism does not depend on the pressure difference because the formation of bubbles can barely be realized.

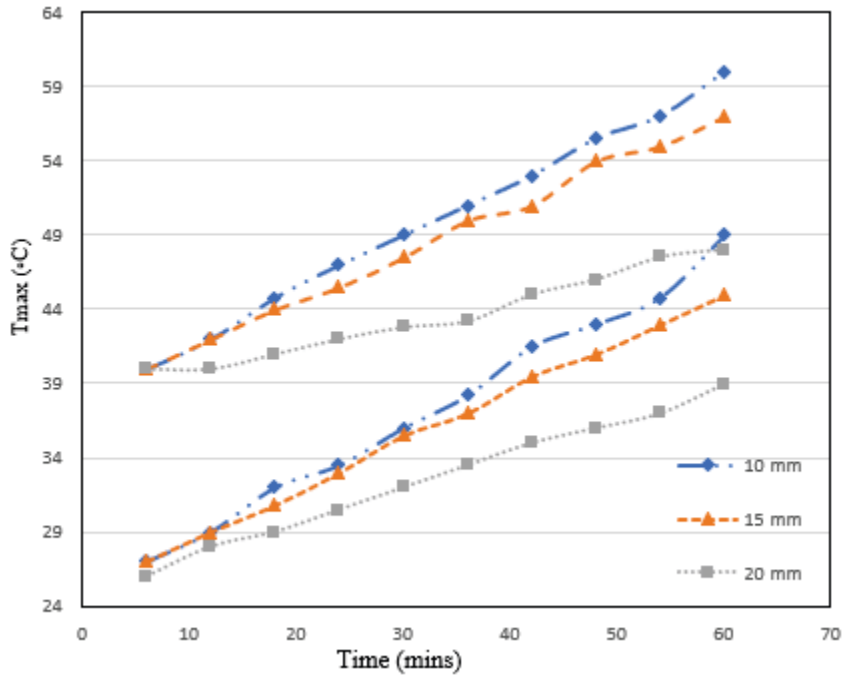


Figure 4.5 Battery temperature profile with different condenser lengths at both standard and abnormal ambient conditions.

A uniform pack temperature is also critical to guarantee the battery system life cycle [28]. The simulation also revealed the ΔT among batteries during the discharge process. When the condenser length was 20 mm, the temperature was uniformly distributed, with the largest ΔT of 1.2 °C, as illustrated in Fig. 4.6. Both 10 mm and 15-mm condenser lengths had a significant temperature difference of 2.2 °C and 2 °C under the mild ambient temperature (25 °C). A 2 °C variation is equivalent to a 10% difference when the pack temperature increases by 20 °C. With this consideration, both 10 mm and 15-mm are unacceptable. The same analogy applied for abnormal conditions, and the ΔT plot is illustrated in Fig. 4.7. ΔT extended to 3 °C and 3.7 °C for 15 and 10 mm, respectively. Since a uniform pack temperature advances the battery life span, given

this, the sensitivity study indicates that the ideal condenser length for the battery pack is 20 mm to guarantee temperature control and prevent severe capacity fading.

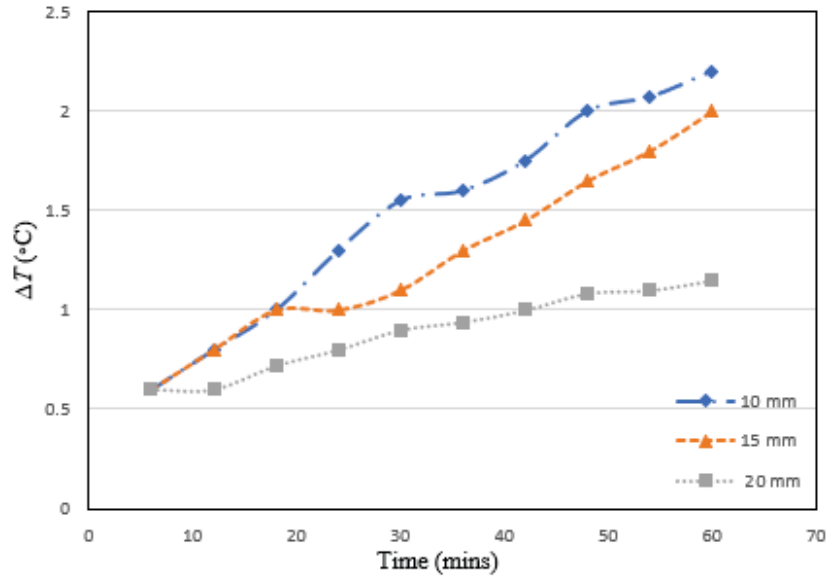


Figure 4.6 Battery ΔT profile with an ambient temperature of 25 °C.

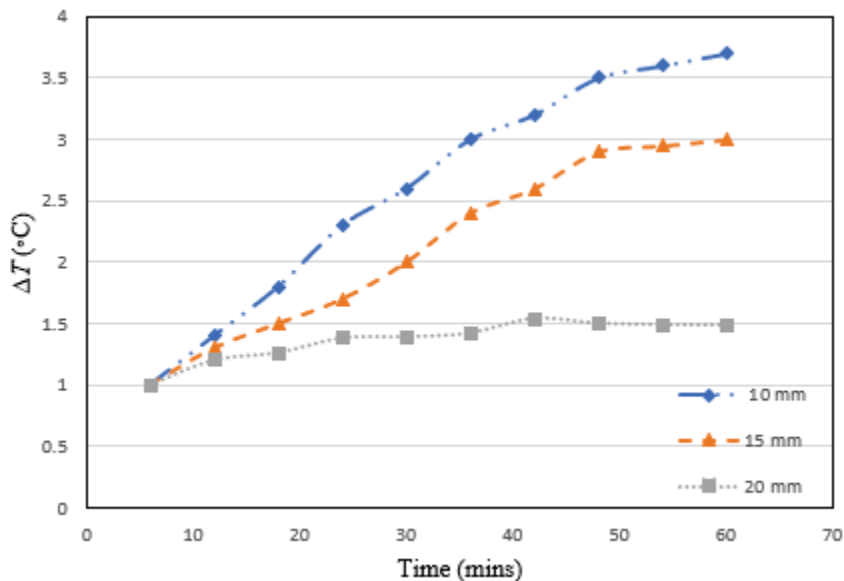


Figure 4.7 Battery ΔT profile with an ambient temperature of 40 °C.

4.2 Comparison of Thermal Management Systems

The comparison study was carried out for five BTM systems: natural cooling, forced air cooling, water channel cooling, traditional heat pipes, and the PHP-based BTM system. The T_{\max} and ΔT were observed under different usage conditions (i.e., 1C and 2C) to evaluate the performance of these systems.

4.2.1 PHP vs. Active BTM system

Liquid cooling is the most commonly adopted active cooling system with a large specific heat capacity. In this experiment, the PHP was carried from the sensitivity study. The inlet velocity of the water cooling was set to 0.2 m/s, and the fluid inlet temperature was set to 25 °C for both ambient scenarios [29]. Mesh quality for the active liquid cooling system is illustrated under Table 10, where the orthogonal quality is considered excellent due to the mesh geometry and small element size.

Table 10. Mesh quality summary for the liquid cooling system.

| Active liquid cooling | |
|-----------------------|------------|
| Element size (mm) | 0.5 |
| Cell shape | Hexahedron |
| Orthogonal quality | 0.999 - 1 |
| Number of nodes: | 15,618,485 |

Fig. 4.8 illustrates the T_{\max} along the discharge time. The PHP was less efficient than water channel cooling as the highest temperature was 39 °C and T_{\max} by liquid cooling was 35.8 °C. However, the necessity of PHP is illustrated in the plot, where T_{\max} by natural cooling ($10 \text{ W m}^{-1} \text{ K}^{-1}$) reached 50 °C. In order to validate the simulation results, a similar test was conducted by Chen *et al.* found the direct liquid cooling restrained the battery temperature elevation within 3 °C under

a 16-minute discharge [40]. Liquid cooling is efficient; however, the simulation set the inlet velocity as 0.2 m/s in each pipe and the outlet as total outflow; in this case, the pressure drop and frictional loss were negligible. In the application, to guarantee a velocity of 0.2 m/s requires pumps and a compensator through the pipe; increasing power consumption is a drawback for active liquid BTM systems.

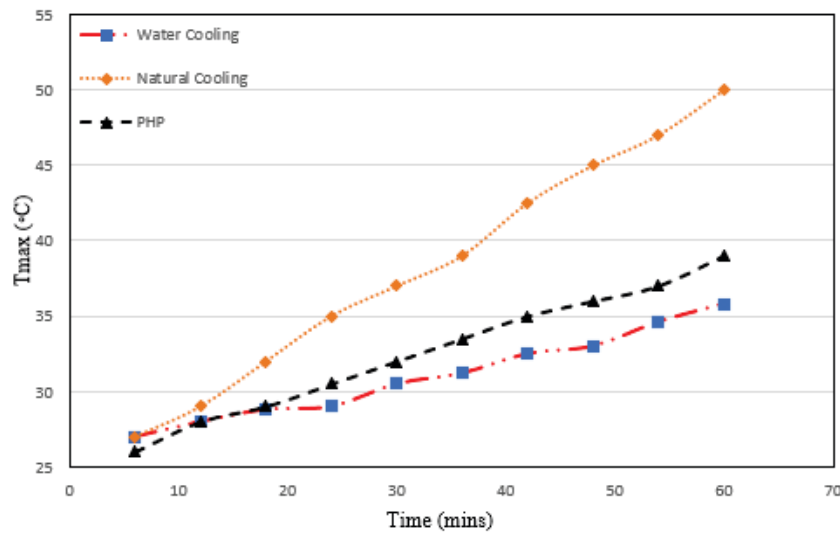


Figure 4.8 Battery temperature vs. time profile for PHP and liquid cooling at a discharge rate of 1C, at an ambient temperature of 25 °C.

In the extreme ambient temperature condition (40 °C), when the conduction through the PHP wall inputs higher energy, two-phase flow forms earlier than in the mild ambient case (25 °C), resulting in the PHP having a similar performance in the liquid cooling experiment. Both management systems worked efficiently and retained the pack temperature within 50 °C. As Fig. 4.9 illustrates, the difference of T_{\max} between liquid cooling and PHP was only 3 °C, where the natural cooling resulted in the T_{\max} of 62 °C. As the T_{\max} observed by PHP was 48 °C (below the

pass criteria), with less space and power consumption, the designed passive system was adequate for thermal surge control when handling large battery packs. In terms of real-world applications, five PHPs for a 2-kWh battery pack are considered feasible and optimal.

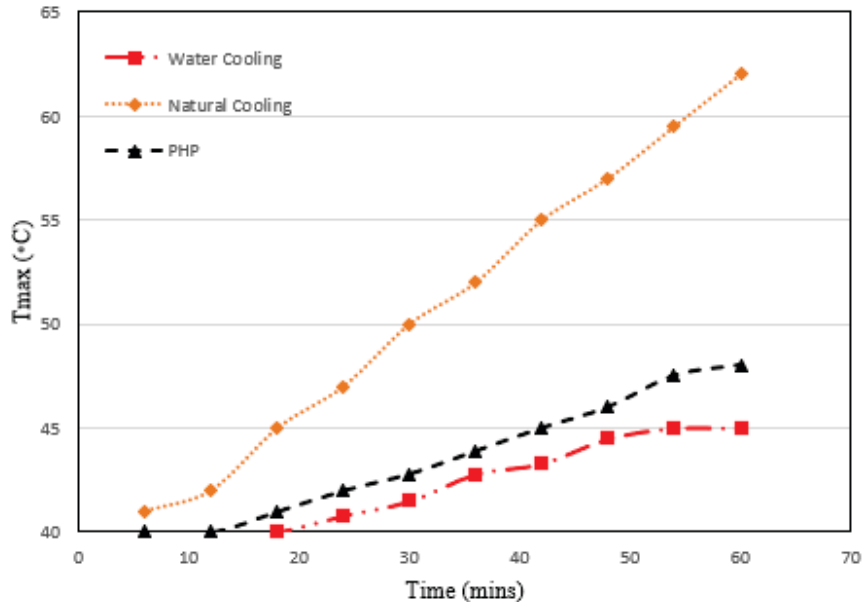


Figure 4.9 Battery temperature vs. time profile for PHP and liquid cooling at a discharge rate of 1C, at an ambient temperature of 40 °C.

Active air-cooling is easier to realize with a higher safety index. Air cooling was simulated via a wind tunnel, and battery packs were placed within the tunnel. Air inlet velocity was set to 1 m/s; with the thermal model calculation, the forced convection coefficient reached around $30 \text{ Wm}^{-2} \text{ K}^{-1}$ [33]. The mesh quality is summarized in Table 11 since the mesh geometry for the air-cooling channel is observed as a triangular prism that resolves the boundary layer efficiently; however, the orthogonal quality is a bit reduced.

Table 11. Mesh quality summary for the forced-air cooling system.

| Active air cooling | |
|--------------------|------------------|
| Element size (mm) | 0.5 |
| Cell shape | Triangular Prism |
| Orthogonal quality | 0.988 - 1 |
| Number of nodes: | 13,472,563 |

Under mild ambient temperature (25°C), Fig. 4.10 shows that air cooling was less effective than the PHP-based system; however, the result was within the acceptable range. The temperature difference in the simulation results of the battery with small-scale PHPs and the active air-cooling system is shown in Fig. 4.111. Airflow is in one direction, and less contact surface is engaged for convection than a PHP-based BTM system, which is considered the main factor that active air cooling is less effective. The vortex generated by front batteries reduced the heat removal rate for the whole battery set [31]. To better understand the air flow pattern inside the air channel, the velocity contour is attached in Fig. 4.12 from both top and side view of the model. As the battery pack 2 to 11 experienced low convection surface area and low velocity, higher ΔT is expected. For PHP, the sidewall of each battery pack is guaranteed to contact the pipe boundary for thermal conduction to promote circulation through PHPs.

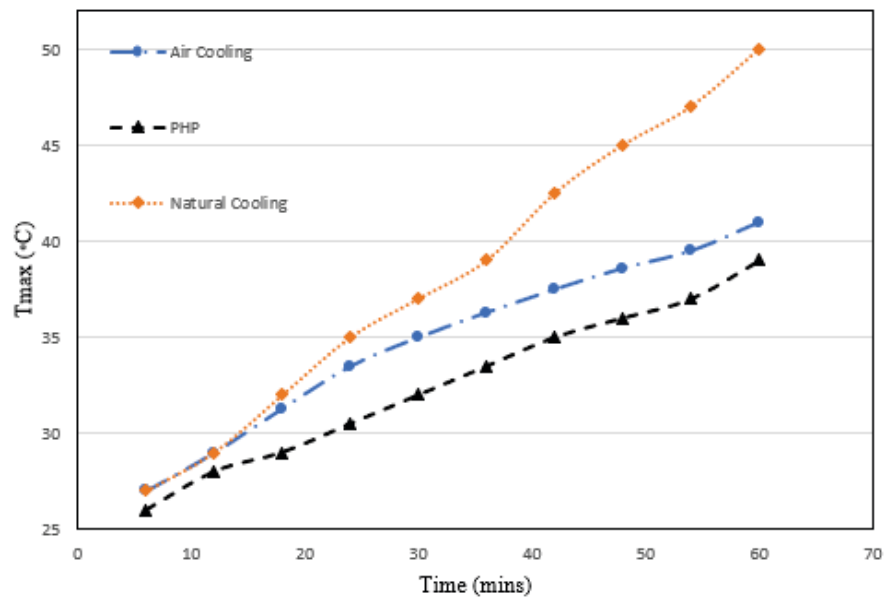


Figure 4. 10 Battery temperature vs. time profile for PHP and air cooling at a discharge rate of 1C, at an ambient temperature of 25 °C.

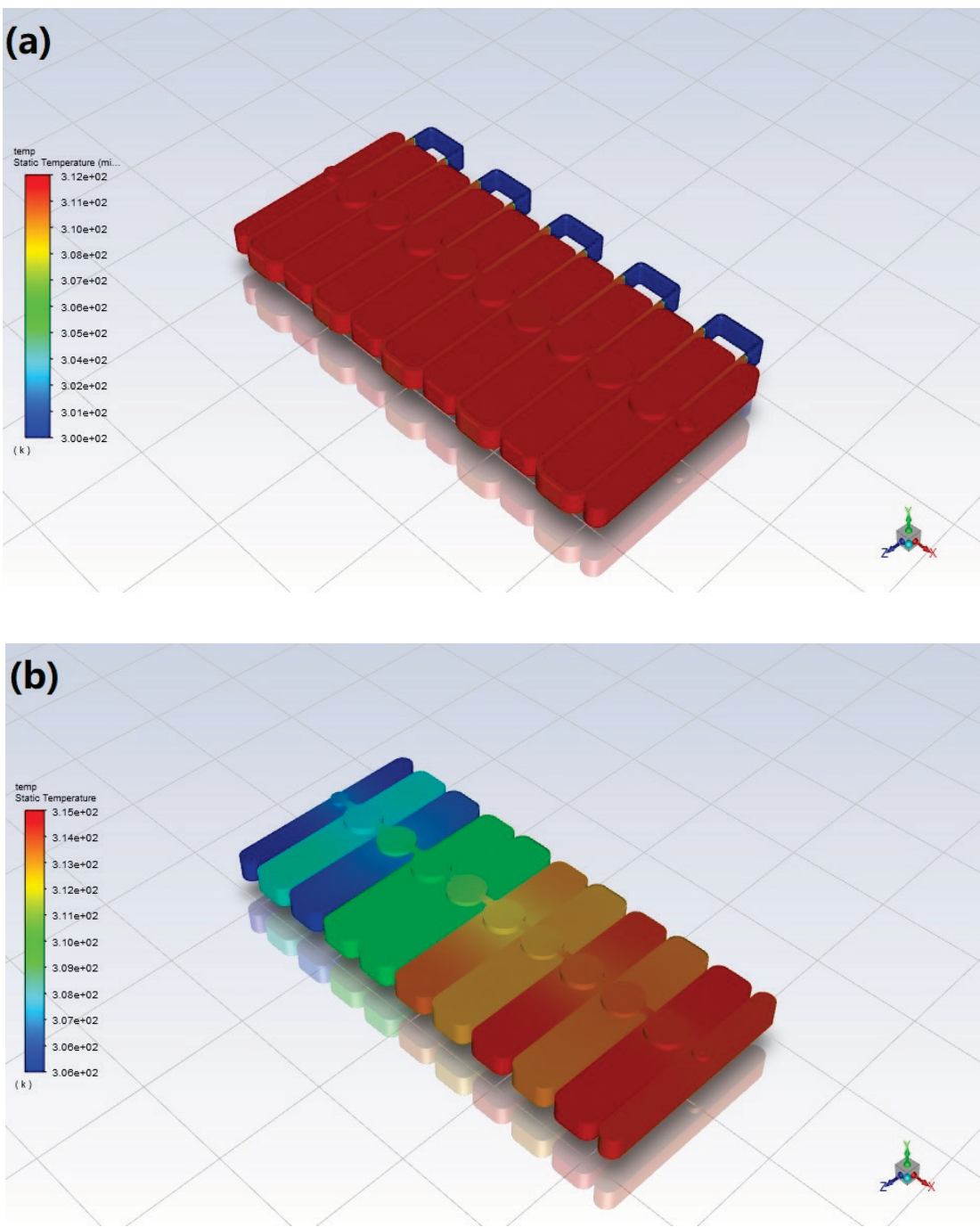


Figure 4.11 Numerical simulation profiles of temperature distribution inside battery pack with (a) PHP-based BTM system; (b) air cooling BTM system at the end of discharge.

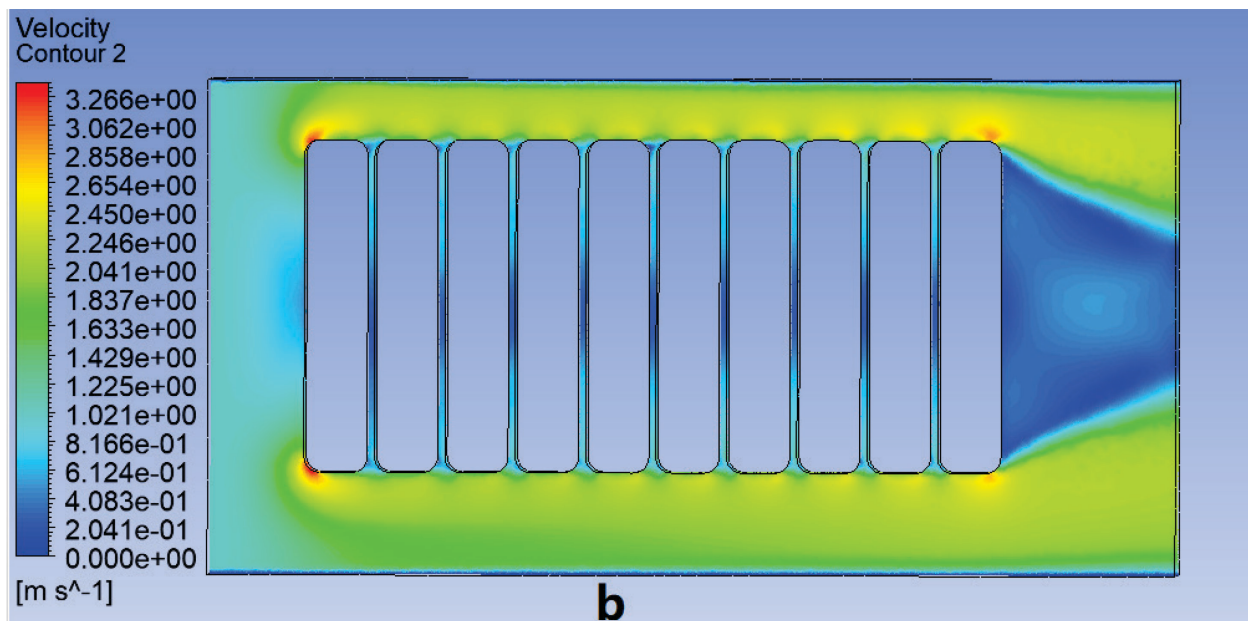
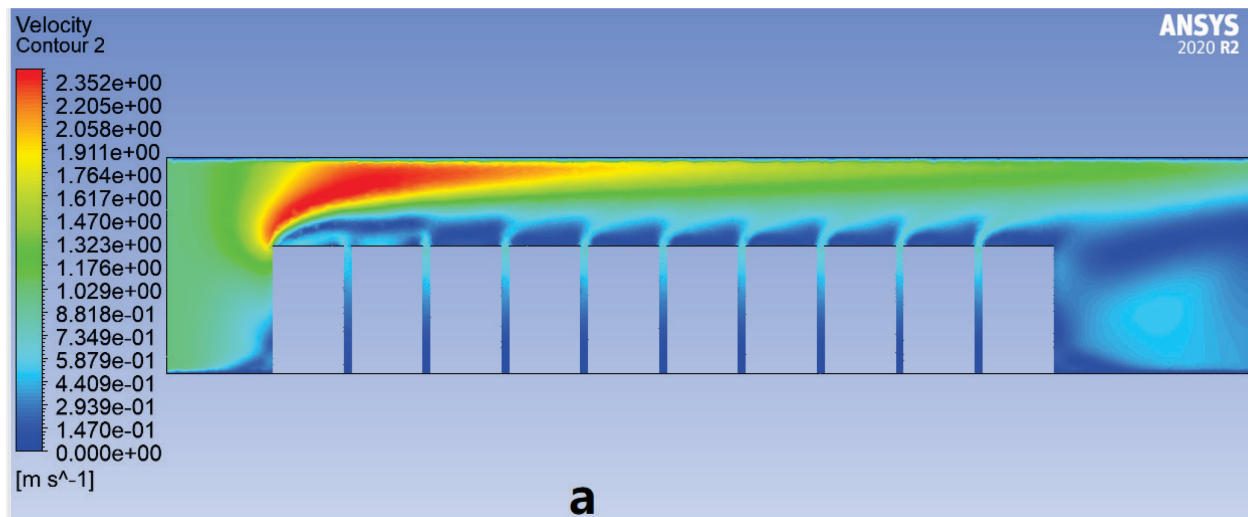


Figure 4.12 Air velocity counter: (a) battery pack side view; (b) Velocity contour from battery pack

top view.

Thermal characteristics for high ambient temperature conditions are shown in Fig. 4.13. The figure depicts that battery T_{\max} via active air cooling was 57°C ; it should not be considered an effective BTM system as it has exceeded the desirable range. Since the heat removal rate by active air cooling is strictly related to the vortex generated within the cabin, ΔT was also investigated to determine the pack temperature, shown in Fig. 4.14. The maximum ΔT in the battery pack experienced by air cooling was approximately 6°C , which is considered a significant temperature variation that could trigger a single battery failure to shorten the battery pack capacity [32]. Pack ΔT under PHP-based BTM system able to maintain at 1.5°C . As the developed BTM system works with a passive cooling mechanism with better performance, thus the system should be applied to handle thermal control with large battery packs.

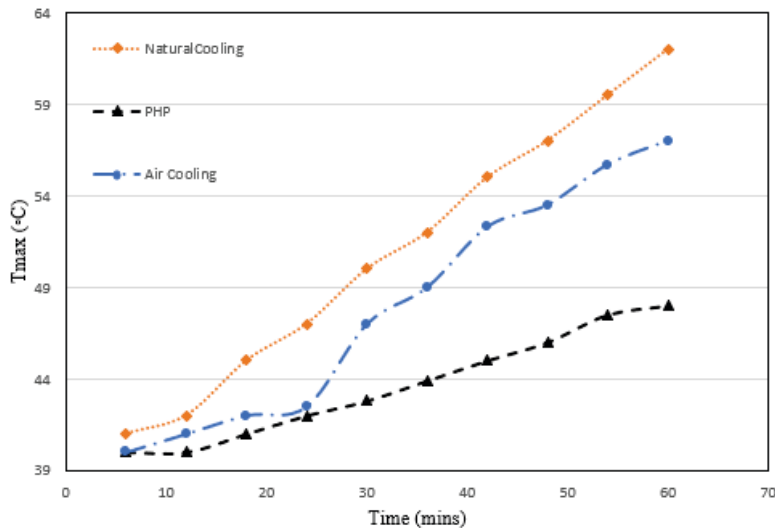


Figure 4.13 Battery temperature vs. time profile for PHP and air cooling at a discharge rate of 1C, at an ambient temperature of 40°C .

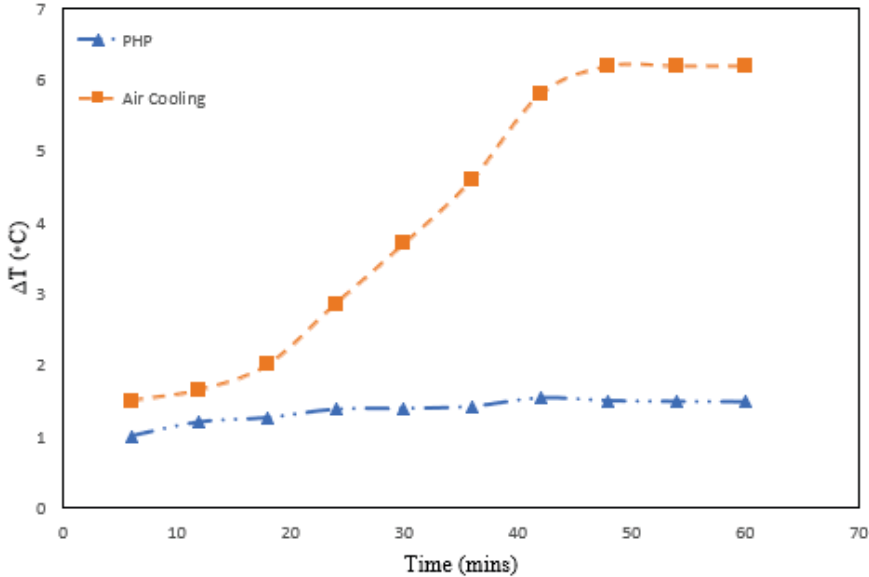


Figure 4.14 Battery ΔT vs. time profile for PHP and liquid cooling at a discharge rate of 1C, at an ambient temperature of 40 °C.

From a design aspect, air cooling is processed by a fan, which affects the leak proofness of the battery pack. Therefore, dust and water could be dragged into the cabin by a fan. Given these considerations, air cooling may not be easy to maintain. In conclusion, PHP is more effective for large battery packs than active BTM systems; the extra power consumption by active cooling would impose challenges to the durability and portability of the battery pack.

4.2.2 PHP vs. Heat Pipes

Traditional heat pipes were used as passive cooling methods in the discharge tests. Fig. 4.15 shows the geometrical configuration of the model used in the simulation. Copper heats pipes are composed of a copper sintered wick tube with a 5 mm width and a wall thickness of 0.5 mm; a sintered wick thickness of 0.3 was constructed. Like in the PHP model, a turbulent multiphase flow system was applied to model the evaporation and condensation of fluid inside the pipe, where

the mass transfer contour is illustrated in Fig 4.16. The transient model of traditional heat pipes verified the high effective thermal conductivity, where provides better thermal control performance on battery packs. From the mesh generator aspect, the mesh quality of traditional heat pipe is similar to small scale pipe, where the same mesh geometry is observed with high quality of the mesh, which is shown in Table 12 . The result of simulation is compared with the study conducted by Wei *et al.* where the result is shown in Table 13 [41]. During 1 C-rate of discharge, 12.57 °C elevation is observed, which verified the simulation accuracy.

Table 12. Mesh quality summary for traditional heat pipe-based cooling system.

| Traditional heat pipe cooling | |
|-------------------------------|------------|
| Element size (mm) | 0.5 |
| Cell shape | Hexahedron |
| Orthogonal quality | 0.999 - 1 |
| Number of nodes: | 14,059,257 |

Table 13. Thermodynamic parameters of the 60 Ah battery cell at different rates [41].

| rate | charge process | | discharge process | |
|-------|-----------------------|-------------------|-----------------------|-------------------|
| | temperature rise (°C) | heating power (W) | temperature rise (°C) | heating power (W) |
| 1/3 C | 9.75 | 2.06 | 10.01 | 2.56 |
| 2/3 C | 10.73 | 2.95 | 11.15 | 3.12 |
| 1 C | 12.57 | 5.42 | 15.28 | 7.60 |
| 1.5 C | 18.94 | 10.06 | 23.27 | 15.59 |
| 2 C | 22.62 | 14.44 | 26.99 | 19.89 |

The results illustrated in Fig. 4.17, heat pipes were effective under mild ambient temperature, which lowered the T_{max} by 2.5 °C than the PHP-based system. Heat pipe working temperature starts at 15 °C where is much lower than developed PHP, which is the main reason that the performance

by traditional heat pipes is outstanding under mild ambient conditions. However, under abnormal ambient conditions, heat pipes showed results that were similar to the small-scale PHPs. The reason to have this phenomenon is because of the excessive heat generated by the battery pack. The small-scale PHP generally absorbs more heat from the specific heat capacity perspective due to the high filling ratio, where the least efficient case would turn the PHP into a single-phase thermosyphon. During the simulation, each battery pack carries 205 Wh, which is dissipated by 2 heat pipes. According to Celsia, the maximum heat pipe power carrying capacity for a 5 mm heat pipe is around 65 W [34]. Given this information, heat pipes do not act as an effective BTM system when encountering an enormous input power. Heat pipes are not recommended as the passive BTM system under abnormal conditions due to a high possibility of dry out. Moreover, to improve the efficiency of the capillary capacity wick structure is expected to be fine enough with a smaller diameter; thus, the cost of heat pipes is higher due to the requirement of wick structure.

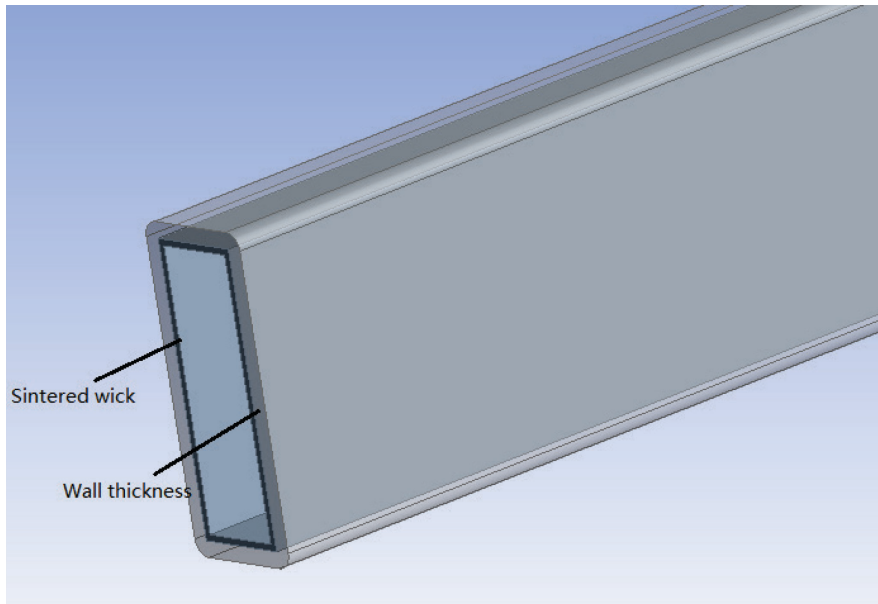


Figure 4. 15 Model geometry of heat pipe.

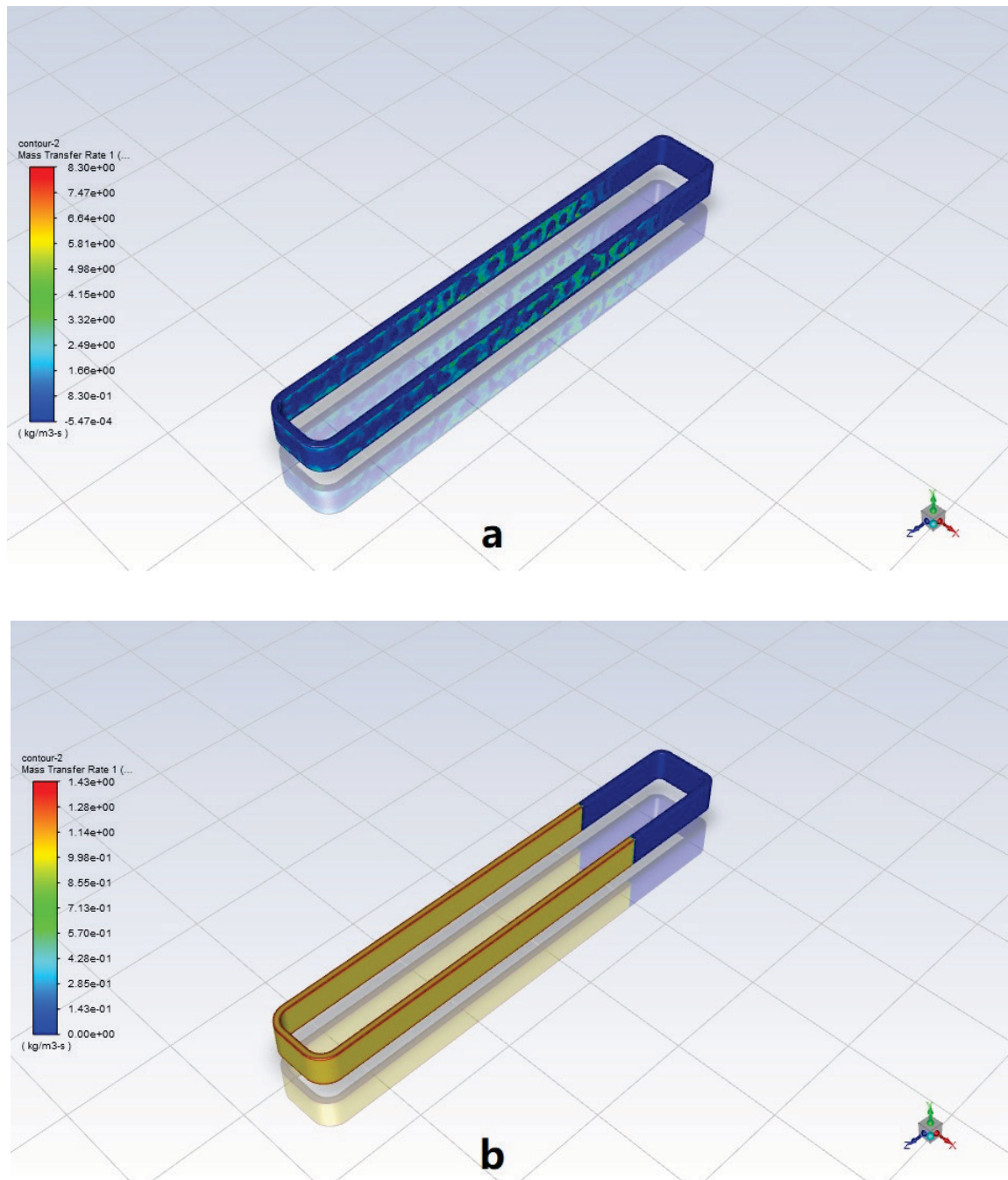


Figure 4. 16 Mass transfer contour with respect to simulation time: (a) $t = 0.3$ s; (b) $t = 3$ s.

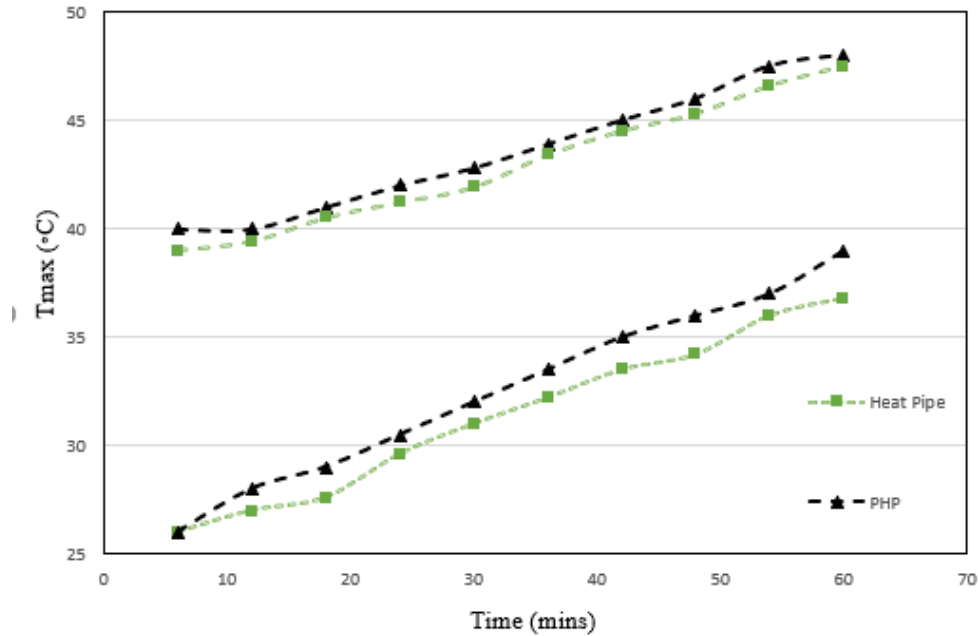


Figure 4. 17 Battery temperature vs. time profile for PHP and heat pipes at a discharge rate of 1C, with different ambient conditions.

4.3 Summary

This chapter compares thermal management systems between natural cooling, active cooling, traditional heat pipes, and the developed PHP-based system. Based on simulations, small-scale PHP has an efficient heat removal performance that matches the liquid cooling and performs better than air cooling. The advantage of using the PHP-based BTM system is to achieve low Tmax under different ambient conditions and maintain uniform pack temperature to prevent capacity fading. The minimum condenser length for the PHP-based system was observed at 20 mm; meanwhile, the recommended wall thickness is 1 mm to provide a similar performance as traditional heat pipe.

Chapter 5: The Evaluation of Large Pulsating Heat Pipe Cooling

Performance on Li-ion Battery

Maximizing a single heat pipe size is essential for practicality in real-world applications, as liquid cooling for a large battery pack is easily achieved by a single loop. However, the same application on heat pipes has hardly been conducted. The simulation for a single PHP compares battery T_{max} and ΔT to existing active BTM systems. The same battery pack from the previous specification was used for the simulation. The simulation was conducted under different ambient usages with a 1 C discharge rate. Considering the actual discharge rate when EVs accelerate, 2 C-rate was also conducted for a 20-minute cycle simulation to test the most severe usages. The comparison between large-scale PHP, water cooling, and air cooling is discussed. Lastly, a summary to address the feasibility of large-scale PHP by considering its thermal performance.

5.1 Pulsating Heat Pipe Simulation

In the first set of simulations, the ambient temperature was set to 25 and 40 °C for mild and abnormal ambient temperatures, respectively. The schematic of the large-scale PHP is illustrated in Fig. 5.1, and the mesh quality summary is included in Table 13. As the working mechanism of the PHP requires condenser sections to achieve two-phase flow, each PHP requires two cooling ends to ensure the condensation can be processed. Noticeably, the condensation cannot be guaranteed for the PHP on packs 1 and 11 due to the geometrical arrangement. Heat removal rate could be affected since the vapor bubbles cannot be condensed sufficiently. Higher T_{max} and ΔT are expected under this layout.

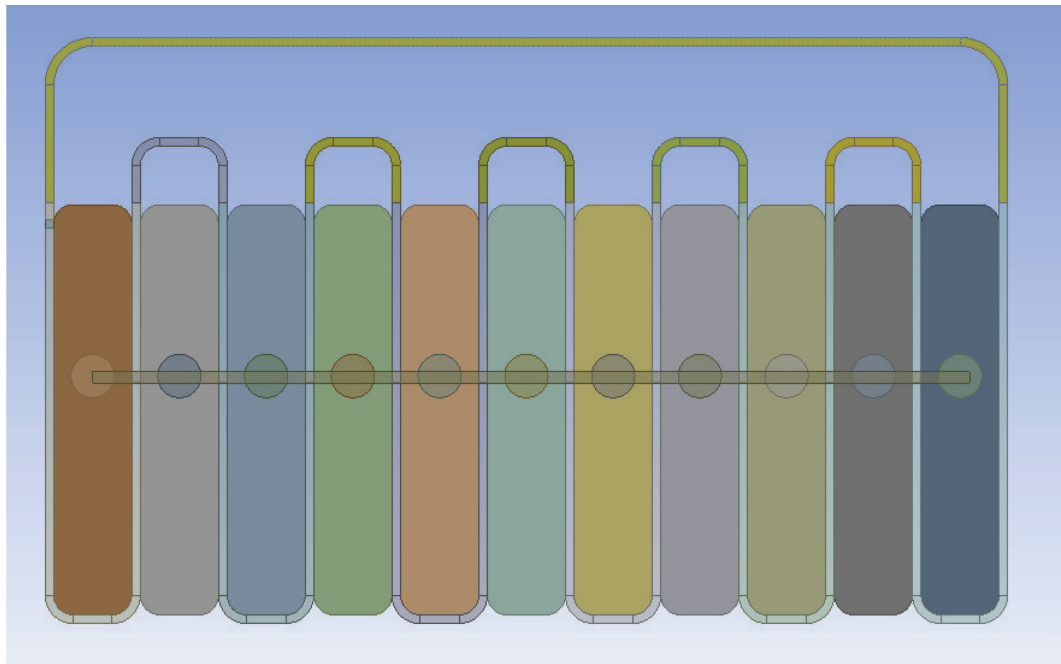


Figure 5.1 Large Scale Pulsating Heat Pipe Geometry.

Table 14. Mesh quality summary for large-scale PHP-based cooling system.

| Large-scale PHP cooling | |
|-------------------------|------------|
| Element size (mm) | 0.5 |
| Cell shape | Hexahedron |
| Orthogonal quality | 0.999 - 1 |
| Number of nodes: | 15,893,962 |

The two-phase flow regime under large-scale PHP is validated under transient heat transfer before the conjugate simulation model. The following figures are the change of water and steam volume fraction inside the pipe, which is attached in Fig. 5.2, and the change of volume fraction on steam validates the PHP functionality, which is illustrated in Fig. 5.3.

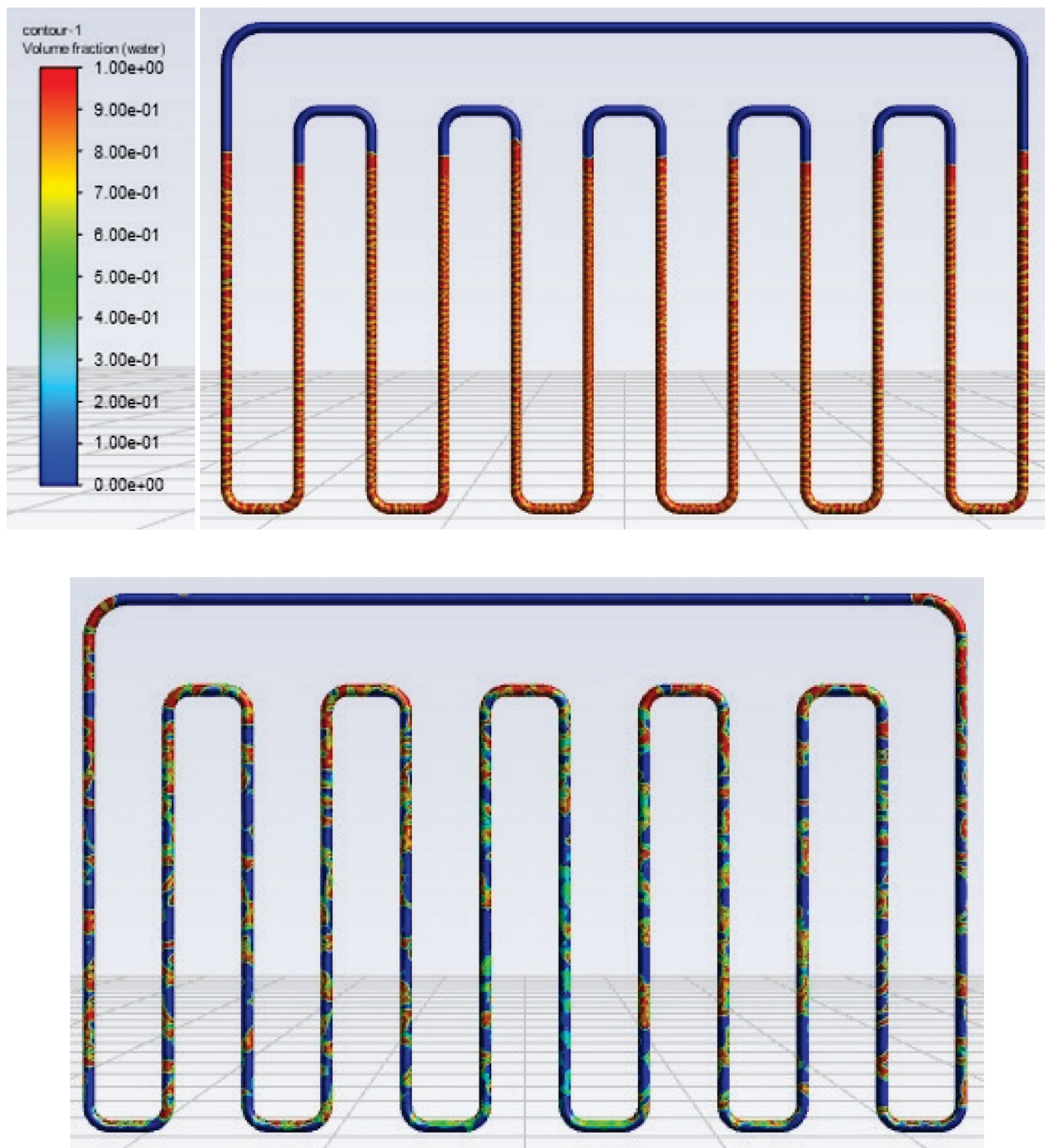


Figure 5. 2 Water distribution at $t = 1$ s, 12 s.

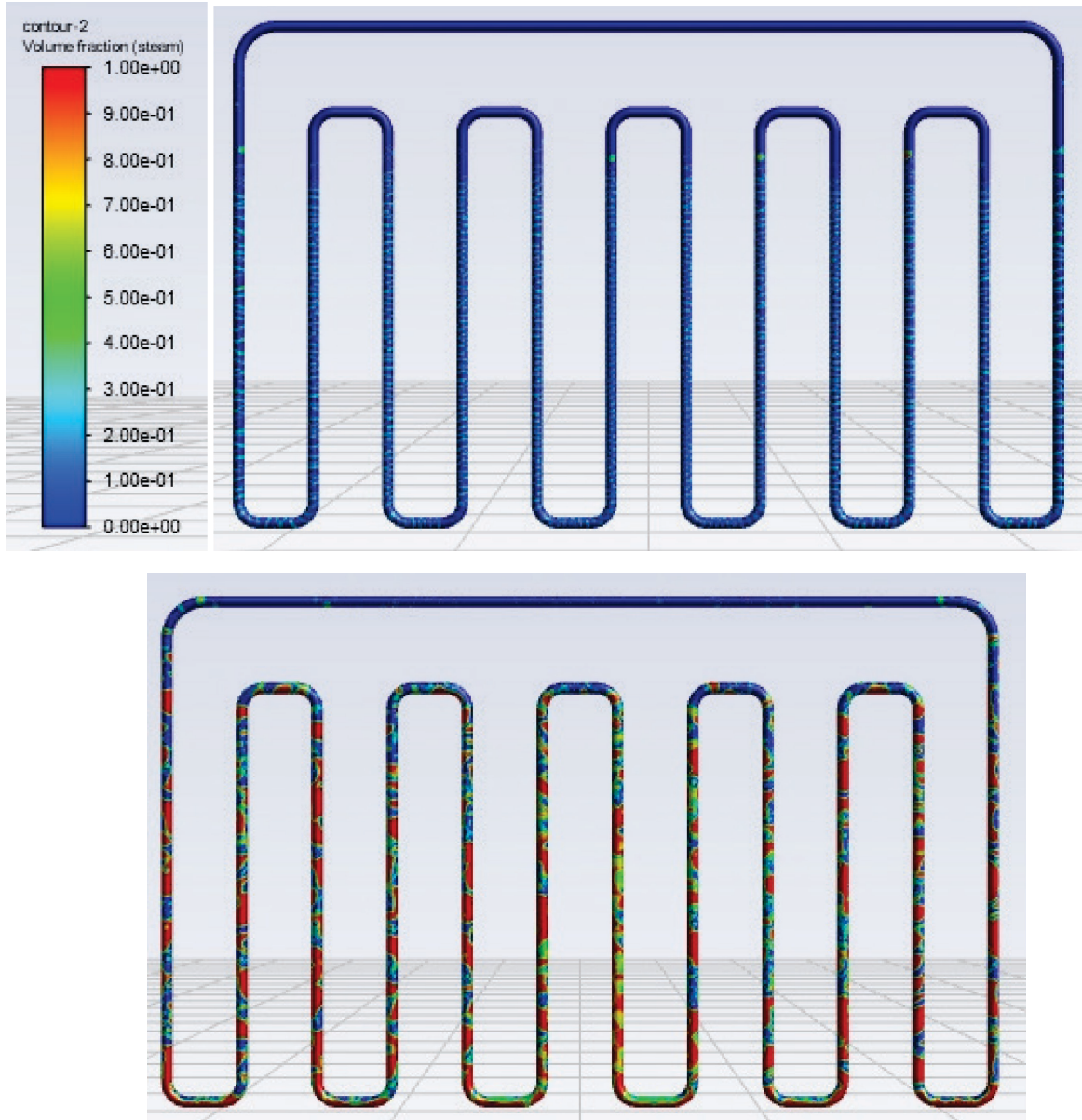


Figure 5.3 Steam Distribution at $t = 1$ s, 10 s.

Fig. 5.4 depicts the temperature curve along time under both ambient conditions, where the highest battery temperatures are 45 °C and 55.5 °C under different ambient temperatures, respectively. The temperature control was still effective compared to the battery under natural cooling (T_{max} at 50 °C and 60 °C). However, compared to the T_{max} , when small-scale PHP is applied, the T_{max} was only 39 °C and 48 °C. The scale of the temperature rise was unexpected; moreover, as shown in Fig. 5.5, the ΔT for large-scale PHP elevation was much more significant. Battery

temperature experienced a maximum ΔT of $2.5\text{ }^{\circ}\text{C}$ and $3.23\text{ }^{\circ}\text{C}$, nearly doubling the ΔT when the small-scale PHP was employed.

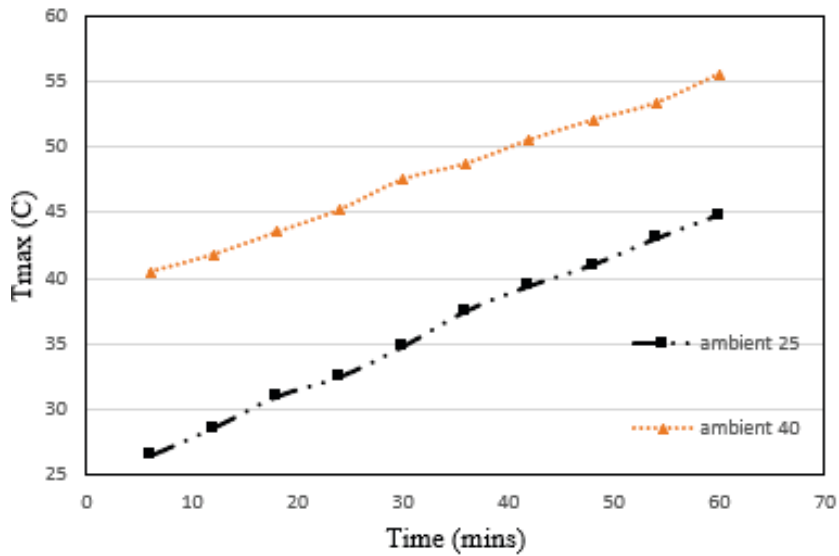


Figure 5.4 Temperature curve under 1C discharge rate.

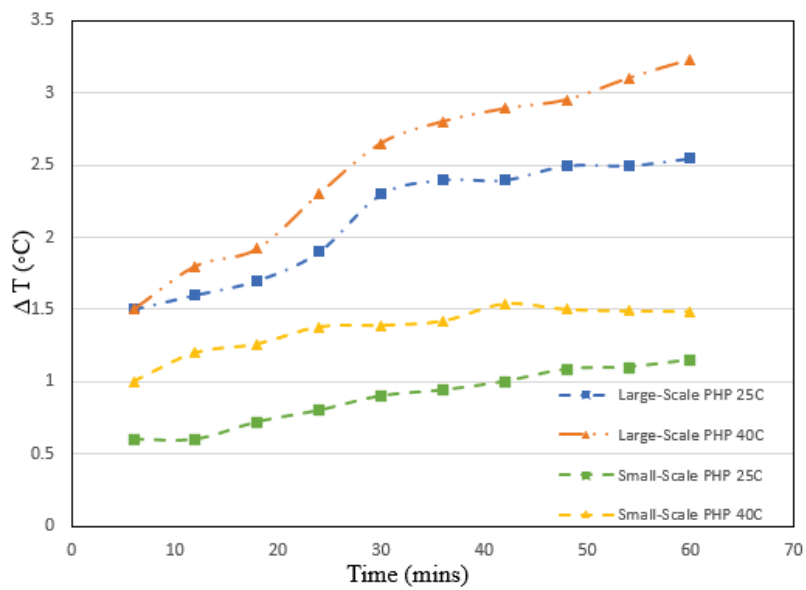


Figure 5.5 Temperature difference comparison on small-scale PHP vs. large-scale PHP.

The comparison of different systems under the 1C discharge rate is illustrated in Fig. 5.6. The plot was constructed to consider the T_{max} , which accounts for the battery pack 1 and 11 in large-scale PHP. Both active methods provided a significant convection coefficient under mild ambient temperature conditions (air: 30 W m⁻² K⁻¹, liquid: 0.03 Kg s⁻¹). When considering the system's average temperature (42.5 °C), the temperature performance was similar to active air cooling. For large-scale PHP, temperature control was less effective than active thermal management systems; however, it was still feasible to control the temperature within the suggested operating temperature (≤ 50 °C).

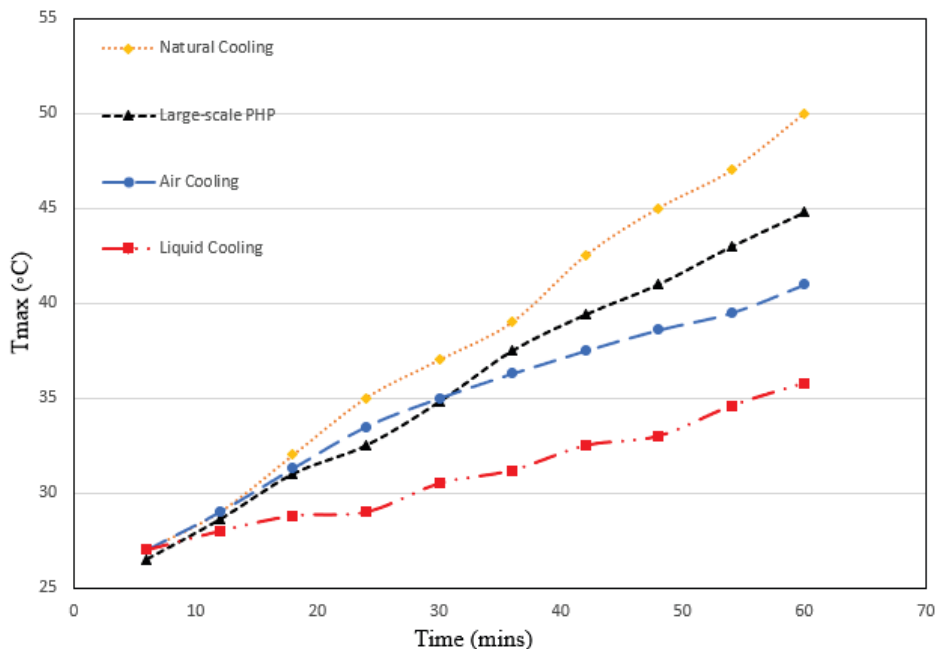


Figure 5.6 Temperature performance with different cooling methods at 25 °C.

Fig. 5.7 represents the results when simulated under an abnormal ambient temperature; large-scale PHP becomes more effective than air cooling but is still not feasible for practical use compared to active liquid cooling. In this scenario, T_{max} was controlled at 55.5 °C, which is 1.5

degrees lower than air cooling. Compared to the T_{\max} was 62°C when only natural convection was applied, the temperature variation of 6.5°C with an average pack temperature of 54°C by large-scale PHP is acceptable but not recommended. A significant flow rate without losses is why active liquid cooling is the most effective with minor temperature rise and operating conditions.

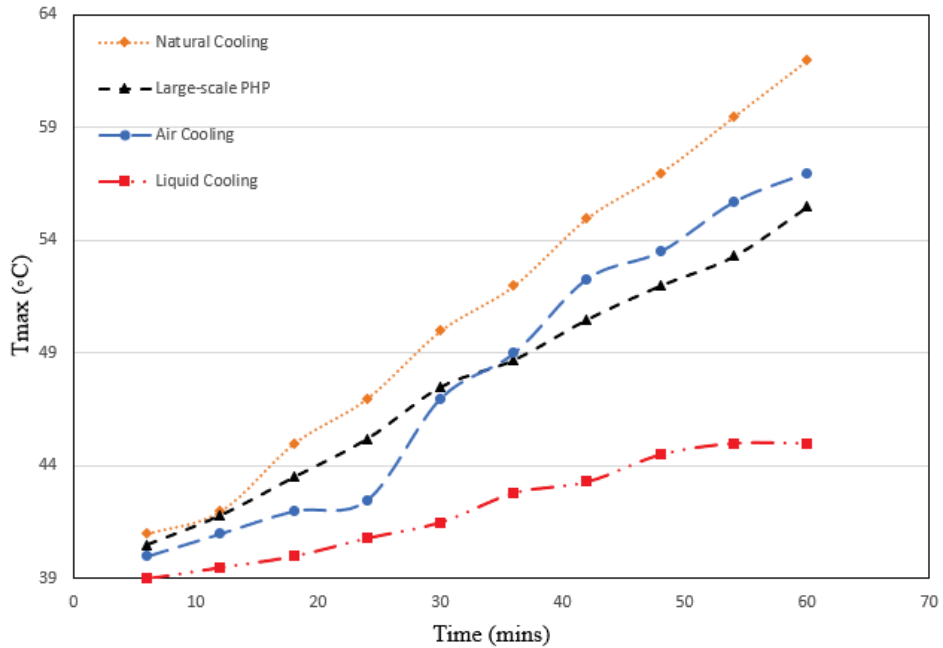


Figure 5.7 Temperature performance with different cooling methods at 40°C .

According to Saxena, during the acceleration of EVs, the battery discharge rate reaches 1.5 C-rate to 2 C-rate [35]. A 2 C-rate discharge test should be proceeded as the thermal abuse condition to test the system's performance. The simulation was conducted for 20 minutes for all BTM systems to compare results and is shown in Fig. 5.8. Large-scale PHP maintained the T_{\max} at 43°C , which is efficient enough compared to the battery with natural cooling ($T_{\max} 55.2^{\circ}\text{C}$). As the battery discharge rate was increased, air cooling became insufficient to reduce the battery temperature due to a relatively low convection coefficient. The T_{\max} by air cooling was observed as 49.5°C , or 6.5 degrees higher than PHP cooling, which is unacceptable as it has exceeded the

pass criteria. Liquid cooling control T_{max} at only 39 °C; however, both liquid cooling and PHP had similar ΔT among the battery packs. These results indicate that PHP acts as an intermediate solution for battery pack heat dissipation and provides uniform pack temperature while consuming less power.

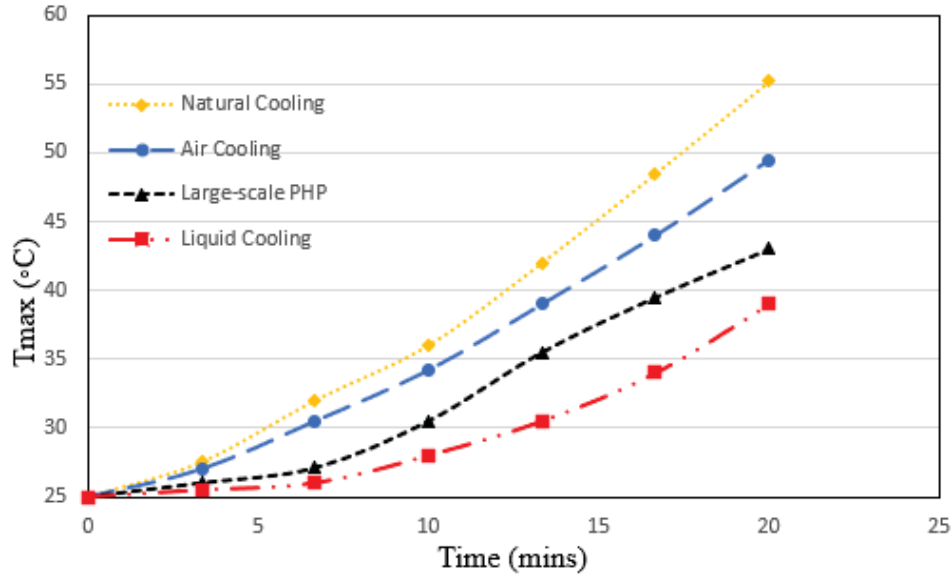


Figure 5.8 Battery temperature simulation of 2 C-rate under different systems at 25 °C.

The last simulation set was conducted for the abnormal ambient temperature, considered the most severe usage condition due to the elevated temperature and high discharge rate shown in Fig.5.9. From the simulation, the PHP became unfavorable; after 20 minutes of discharge, the highest temperature reached 62 °C, which exceeded the maximum allowance range by 12.7%. In real-life applications, considering the temperature delay, the rise is expected to continue even the discharge has stopped. Similar results were observed from the air-cooling system, where T_{max} reached 71 °C. Under this thermal abuse model, even liquid-cooling presented an elevation of 13 degrees under the 20-minute discharge.

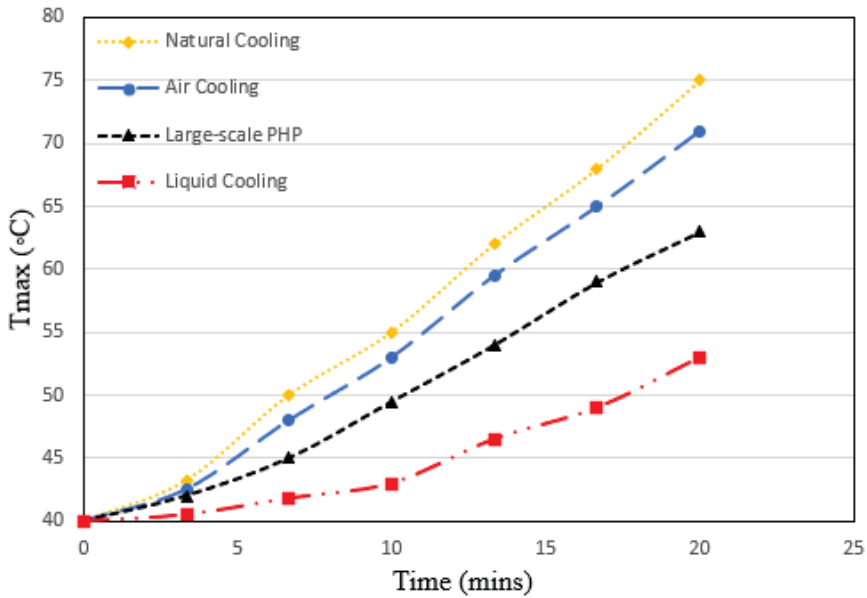


Figure 5.9 Battery temperature simulation of 2 C-rate under different systems at 40 °C.

The last discussion is the effect of fluid material on simulation results, as the simulation is conducted by using water liquid and water vapor for PHPs. However, in the application, EVs are expected to experience weather conditions around -25 °C in winter. Thus, ethanol is considered a more suitable medium for PHP. The thermal management performance of two different fluids was conducted to test the maximum temperature of the battery at a 1C discharge rate with two different ambient temperatures. The maximum temperature under two simulations remained the same for two different fluids with different boiling points and surface tensions. Studying fluid thermal resistance is essential to understand the phenomenon. Pachghare *et al.* investigated the thermal performance of different fluids for PHP, including pure fluids such as methanol, water, acetone, and ethanol [36]. The authors also investigated binary fluids, including water/methanol, water/acetone, and water/ethanol. Pachghare *et al.* found that the thermal resistance of ethanol and water is equivalent when the heat input is higher than 90W [36]. The illustration of power input

vs. thermal resistance of fluid is included in Fig. 5.10. In the current simulation, each small battery pack contains total energy of 205 Wh. The heat generated by the battery pack has exceeded the critical value (90 W) under the 1 C-rate discharge. Since the definition of thermal resistance is $^{\circ}\text{C}/\text{W}$, which is the temperature change due to the imposed power. Thus, with the substantial input power, temperature elevation remained the same for different mediums, resulting in the same heat removal rate.

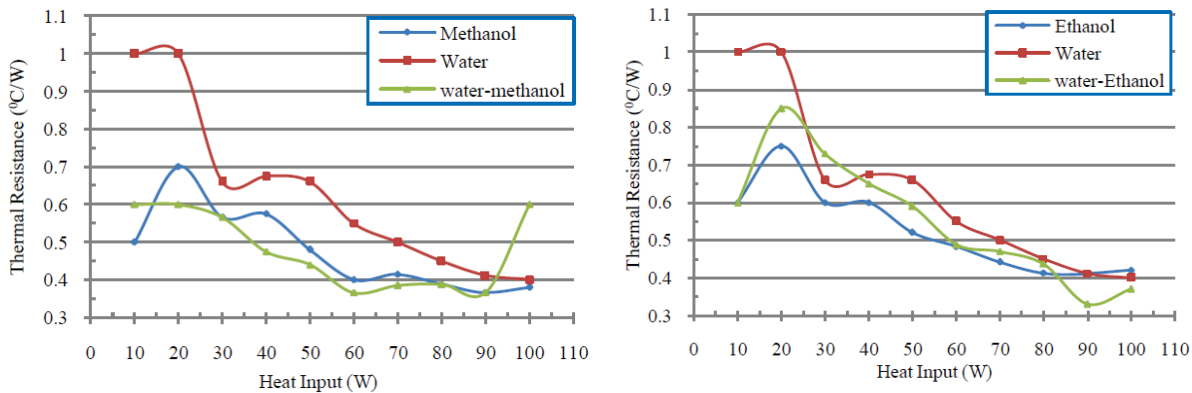


Figure 5.10 Thermal resistance of different fluids for PHPs [27].

5.2 Summary

Large-scale PHP was tested for both standard and abnormal ambient temperatures. The objective was to observe the battery pack control via large-scale PHP and compare it to other active cooling systems.

- 1) Large-scale PHP was expected to lead to higher pack temperature, as packs 1 and 11 from the system could not be condensed efficiently. Despite these two packs, the average temperature and ΔT of battery packs were still optimal.
- 2) A large ΔT was observed from high ambient temperatures. Findings from the comparison study suggest that a large-scale PHP is still practical to restrain the pack temperature; however, a large-scale PHP is not more efficient enough than liquid cooling. Although a large-scale PHP was more effective than air cooling; however, the performance was not practically meaningful under abnormal usage conditions. Considering the external power consumption and the fabrication difficulty of active BTM systems, large-scale PHP is recommended as the BTM system under a compact design consideration.
- 3) PHP maintains the same performance with a different medium. The study revealed that the performance of the PHP is affected by the power input through the boundary wall. The substantial heat generated by the battery pack, methanol, ethanol, and water shows the same thermal resistance, indicating that the materials have the same thermal conductivity.

Chapter 6: Conclusion and Future Works

The review of the passive PHP-based thermal management system and the results from all simulations are concluded. Furthermore, the expected future work to continue this passive cooling system is also provided.

6.1 Conclusion

This thesis focused on developing a passive PHP-based BTM system. The simulation was first conducted by applying a small-scale PHP, which requires five individual PHPs to achieve heat dissipation on a 200-battery pack. The two-phase flow continues its way toward the condenser section, where bubbles are collapsed, emitting latent heat of vaporization. With the success of the small-scale PHP, a large PHP was tested by using a single pipe to circulate the whole battery pack. Both PHPs were compared to active cooling systems under different usage conditions. Few remarks are summarized below:

- (1) The sensitivity study was performed to identify the minimum condenser length and the ideal PHP dimensions. The suggested setup for wall thickness is 1 mm, and 20 mm for condenser length.
- (2) Small-scale PHP is more effective by providing lower battery temperature, and a smaller ΔT . Small-scale PHP showed similar performance to traditional heat pipes and liquid cooling for temperature control under both ambient conditions.
- (3) The application scale of traditional heat pipes is restricted due to the porous wick structure. Large-scale PHP is conducted to achieve temperature control on an extensive power pack. Under the large-scale PHP simulation, performance on temperature control became less efficient due to the condensation being inevitably imperfect on the designated battery pack. The battery T_{max} did

not differ significantly between the large-scale PHP and air cooling. However, the feasibility of large-scale PHP is optimal when considering the system's average temperature.

- (4) Under the thermal abuse model, PHP is the best trade-off between performance and power conservation. Air cooling is unacceptable due to the poor convection coefficient, as more power consumption is needed to enhance the convection. Under this circumstance, PHP is recommended as it balances power consumption and thermal performance.
- (5) Heat transfer inside the PHP was not as instant as in a traditional heat pipe; however, PHPs avoid dry out and endure higher power input due to the large filling ratio. Meanwhile, without the wick structure, the cost of PHPs is much lower than for traditional heat pipes.

In conclusion, the developed PHP-based BTM system targets a large battery pack that requires less power consumption and space constraints. Compared to active cooling systems, with the absence of pumps and motors, the developed PHP-based BTM system requires less space and power to maintain pack temperature within the acceptable range. This system can be implemented for both open and closed structures to promote the diversity of the application. The working medium is flexible to change to handle different usage conditions, but similar performance results can be guaranteed.

6.2 Future Works

While this thesis carried out simulations of PHP, real-life experiments are needed. For example, feasibility and functionality tests for large cycles in real-world experiments are necessary to confirm the results of the current study. Some future work can be conducted in the following subjects:

(1) Customization. The design system was only focused on the cylindrical battery pack. With the wide application of Li-ion batteries, power packs are adopted into different volumes, heat generation rates, working environments. Therefore, the performance of different PHP scales should be conducted, which varied in shape, size to meet the specific requirements.

(2) Control and automation. The operating conditions and state of health easily affect the battery thermal behavior, resulting in the change of heat generation rate. An automatic control system should be added to detect the temperature at different locations and adjust the convection condition on PHPs condensation side.

(3) Cold ambient conditions. With challenging temperature conditions, when the battery temperature is below 0 °C, a heating system is needed to guarantee the functionality of the battery. PHP should be developed to provide an optimal operating environment. The PHP-based BTM systems should be used in developing such a heating system.

Bibliography

- [1] X. M. Xu and R. He, “Research on the heat dissipation performance of battery pack based on forced air cooling,” *Journal of Power Sources*, vol. 240, pp. 33–41, Oct. 2013, doi: 10.1016/j.jpowsour.2013.03.004.
- [2] A. Tang, J. Li, L. Lou, C. Shan, and X. Yuan, “ Applied Thermal Engineering,” vol. 159, p. 113760, Aug. 2019.
- [3] K. Li, J. Yan, H. Chen, and Q. Wang, “Water cooling based strategy for lithium-ion battery pack dynamic cycling for thermal management system,” *Applied Thermal Engineering*, vol. 132, pp. 575–585, Mar. 2018.
- [4] G. Saldaña, J. I. San Martín, I. Zamora, F. J. Asensio, and O. Oñederra, “Analysis of the Current Electric Battery Models for Electric Vehicle Simulation,” *Energies*, vol. 12, no. 14, p. 2750, Jul. 2019.
- [5] J. Zhao, P. Lv, and Z. Rao, “Experimental study on the thermal management performance of phase change material coupled with heat pipe for cylindrical power battery pack,” *Experimental Thermal and Fluid Science*, vol. 82, pp. 182–188, 2017.
- [6] “Lithium-Ion Battery,” Lithium-Ion Battery - an overview | ScienceDirect Topics. [Online]. Available: <https://www.sciencedirect.com/topics/chemistry/lithium-ion-battery>. [Accessed: 24-Jul-2021].
- [7] Y. Miao, P. Hynan, A. von Jouanne, and A. Yokochi, “Current Li-Ion Battery Technologies in Electric Vehicles and Opportunities for Advancements,” *Energies*, vol. 12, no. 6, p. 1074, 2019.

- [8] Mischa, “How a battery works,” Curious, 05-Mar-2018. [Online]. Available: <https://www.science.org.au/curious/technology-future/batteries>. [Accessed: 24-Jul-2021].
- [9] S. Du, Y. Lai, L. Ai, L. Ai, Y. Cheng, Y. Tang, and M. Jia, “An investigation of irreversible heat generation in lithium ion batteries based on a thermo-electrochemical coupling method,” *Applied Thermal Engineering*, vol. 121, pp. 501–510, 2017.
- [10] “Passive vs. Active Cooling: What’s the Difference?,” SimScale, 14-Jun-2021. [Online]. Available: <https://www.simscale.com/blog/2017/01/active-and-passive-cooling/>. [Accessed: 24-Jul-2021].
- [11] F. Shi, “Catalysis effect on the solid electrolyte interphase (SEI) in lithium-ion batteries,” *Chemistry of Material*, 2020.
- [12] C. Wang, G. Zhang, L. Meng, X. Li, W. Situ, Y. Lv, and M. Rao, “Liquid cooling based on thermal silica plate for battery thermal management system,” *International Journal of Energy Research*, vol. 41, no. 15, pp. 2468–2479, Jul. 2017.
- [13] A. Lewandowski and A. Swiderska-Mocek, “ChemInform Abstract: Ionic Liquids as Electrolytes for Li-Ion Batteries: An Overview of Electrochemical Studies,” *ChemInform*, vol. 41, no. 38, 2010.
- [14] T. Wang, K. J. Tseng, J. Zhao, and Z. Wei, “Thermal investigation of lithium-ion battery module with different cell arrangement structures and forced air-cooling strategies,” *Applied Energy*, vol. 134, pp. 229–238, Dec. 2014.
- [15] H. Sun and R. Dixon, “Development of cooling strategy for an air-cooled lithium-ion battery pack,” *Journal of Power Sources*, vol. 272, pp. 404–414, Dec. 2014.

- [16] R. Zhao, J. Gu, and J. Liu, “An experimental study of heat pipe thermal management system with wet cooling method for lithium ion batteries,” *Journal of Power Sources*, vol. 273, pp. 1089–1097, Jan. 2015.
- [17] R. Zhao, J. Liu, and F. Ma, “A Comprehensive Comparison of the Phase Change Material-Based Internal and External Cooling Systems,” *ECS Meeting Abstracts*, vol. MA2020-01, no. 2, pp. 460–460, 2020.
- [18] B. Fadhl, L. C. Wrobel, and H. Jouhara, “Numerical modelling of the temperature distribution in a two-phase closed thermosyphon,” *Applied Thermal Engineering*, vol. 60, no. 1-2, pp. 122–131, 2013.
- [19] Shadowfax, “evaporation-condensation model: 2D simulation of thermosyphon (closed-domain),” Ansys Learning Forum, 09-May-2019. [Online]. Available: <https://forum.ansys.com/discussion/7412/evaporation-condensation-model-2d-simulation-of-thermosyphon-closed-domain>. [Accessed: 24-Jul-2021].
- [20] M. Mameli, M. Marengo, and S. Zinna, “Thermal Simulation of a Pulsating Heat Pipe: Effects of Different Liquid Properties on a Simple Geometry,” *Heat Transfer Engineering*, vol. 33, no. 14, pp. 1177–1187, 2012.
- [21] S. Zhang, “A Hydrogel Based Thermal Management System for Lithium-ion Batteries,” thesis, Carleton University, Ottawa, 2014.
- [22] “Thermal Runaway – What is Thermal Runaway & How to Prevent it: Mitsubishi Electric,” – What is Thermal Runaway & How to Prevent it | Mitsubishi Electric. [Online]. Available: <https://www.mitsubishicritical.com/resources/trends-and-insights/thermal-runaway/>. [Accessed: 24-Jul-2021].

- [23] A. Lewandowski and A. Swiderska-Mocek, “ChemInform Abstract: Ionic Liquids as Electrolytes for Li-Ion Batteries: An Overview of Electrochemical Studies,” ChemInform, vol. 41, no. 38, 2010.
- [24] C.-Y. Tseng, K.-S. Yang, and C.-C. Wang, “Non-Uniform Three-Dimensional Pulsating Heat Pipe for Anti-Gravity High-Flux Applications,” Energies, vol. 13, no. 12, p. 3068, 2020.
- [25] N. N. Kochurova and A. I. Rusanov, “Dynamic surface properties of water: Surface tension and surface potential,” Journal of Colloid and Interface Science, vol. 81, no. 2, pp. 297–303, 1981.
- [26] P. Cheng and H. Ma, “Theoretial sic analysis of oscillating motion, heat transfer, minimum meniscus radius and charging procedure in an oscillating heat pipe,” thesis, University of Missouri--Columbia, Columbia, MO, 2008.
- [27] “Enhanced Wall Treatment,” online.com. [Online]. Available: <https://www.cfd-online.com/Forums/fluent/109837-enhanced-wall-treatment.html>. [Accessed: 24-Jul-2021].
- [28] B.V. Ratnakumar, M.C. Smart, J.O. Blosiu, S. Surampudi. “Storage characteristics of lithium ion cells”. Proceedings of Electrochemical Society 99-25, pp. 706–18, 2000.
- [29] X. Peng, X. Cui, X. Liao, and A. Garg, “A Thermal Investigation and Optimization of an Air-Cooled Lithium-Ion Battery Pack,” Energies, vol. 13, no. 11, p. 2956, 2020.
- [30] N. Z. Ahmed, P. K. Singh, I. Janajreh, and Y. Shatilla, “Simulation of Flow Inside Heat Pipe: Sensitivity Study, Conditions and Configuration,” ASME 2011 5th International Conference on Energy Sustainability, Parts A, B, and C, 2011.

- [31] A. Garg, C. Ruhatiya, X. Cui, X. Peng, Y. Bhalerao, and L. Gao, “A Novel Approach for Enhancing Thermal Performance of Battery Modules Based on Finite Element Modeling and Predictive Modeling Mechanism,” *Journal of Electrochemical Energy Conversion and Storage*, vol. 17, no. 2, 2019.
- [32] F. Leng, C. M. Tan, and M. Pecht, “Effect of Temperature on the Aging rate of Li Ion Battery Operating above Room Temperature,” *Scientific Reports*, vol. 5, no. 1, 2015.
- [33] “Convective Heat Transfer,” Engineering ToolBox. [Online]. Available: https://www.engineeringtoolbox.com/convective-heat-transfer-d_430.html. [Accessed: 24-Jul-2021].
- [34] D. Deng, D. Liang, Y. Tang, J. Peng, X. Han, and M. Pan, “Evaluation of capillary performance of sintered porous wicks for loop heat pipe,” *Experimental Thermal and Fluid Science*, vol. 50, pp. 1–9, 2013.
- [35] X. Feng, M. Fang, X. He, M. Ouyang, L. Lu, H. Wang, and M. Zhang, “Thermal runaway features of large format prismatic lithium ion battery using extended volume accelerating rate calorimetry,” *Journal of Power Sources*, vol. 255, pp. 294–301, 2014.
- [36] “Effect of Pure and Binary Fluids on Thermal Performance of Closed Loop Pulsating Heat Pipe,” *International Journal of Engineering and Advanced Technology*, vol. 9, no. 3, pp. 1716–1721, 2020.
- [37] J. Qu, H. Wu, and P. Cheng, “Experimental study on thermal performance of a silicon-based micro pulsating heat pipe,” *ASME 2009 Second International Conference on Micro/Nanoscale Heat and Mass Transfer, Volume 3*, 2009.

- [38] Y. S. Shekhawat, S. Khandekar, and P. K. Panigrahi, “Hydrodynamic study of an oscillating meniscus in a square mini-channel,” *ASME 2009 Second International Conference on Micro/Nanoscale Heat and Mass Transfer, Volume 2*, 2009.
- [39] H. Barua, M. Ali, M. Nuruzzaman, M. Q. Islam, and C. M. Feroz, “Effect of filling ratio on heat transfer characteristics and performance of a closed-loop pulsating heat pipe,” *Procedia Engineering*, vol. 56, pp. 88–95, 2013.
- [40] D. Chen, J. Jiang, G.-H. Kim, C. Yang, and A. Pesaran, “Comparison of different cooling methods for lithium-ion battery cells,” *Applied Thermal Engineering*, vol. 94, pp. 846–854, 2016.
- [41] T. Wei, X. Xiaoming, D. Hua, G. Yaohua, L. Jicheng, and W. Hongchao, “Sensitivity analysis of the battery thermal management system with a RECIPROCATING Cooling strategy combined with a Flat heat pipe,” *ACS Omega*, vol. 5, no. 14, pp. 8258–8267, 2020.